Int J Adv Manuf Technol
DOI 10.1007/s00170-013-5320-3

ORIGINAL ARTICLE

Investigation of vehicle crash modeling techniques: theory and application

Witold Pawlus · Hamid Reza Karimi · Kjell G. Robbersmyr

Received: 27 March 2013 / Accepted: 17 September 2013

Abstract Creating a mathematical model of a vehicle crash is a task which involves considerations and analysis of different areas which need to be addressed because of the mathematical complexity of a crash event representation. Therefore, to simplify the analysis and enhance the modeling process, in this work, a brief overview of different vehicle crash modeling methodologies is proposed. The acceleration of a colliding vehicle is measured in its center of gravity—this crash pulse contains detailed information about vehicle behavior throughout a collision. A virtual model of a collision scenario is established in order to provide an additional data set further used to evaluate a suggested approach. Three different approaches are discussed here: lumped parameter modeling of viscoelastic systems, data-based approach taking advantage of neural networks and autoregressive models and wavelet-based method of signal reconstruction. The comparative analysis between each method's outcomes is performed and reliability of the proposed methodologies and tools is evaluated.

Keywords Feedforward neural network · Lumped parameter models · Multiresolution analysis · Vehicle crash modeling

1 Introduction

One of the major concerns of the automotive industry is vehicle crashworthiness. Popular rating programs like Euro NCAP or National Highway Traffic Safety Administration are the principal representatives of the organizations which verify whether a given car conform to the safety standards and regulations. One of the biggest challenges related to the vehicle safety assessment process is the proper execution of the experimental crash tests. It is well known that those experiments are complex and complicated ones. For that reason, a lot of efforts have been made to assess the overall car performance during a collision without a need to conduct a full-scale experiment.

Nowadays finite element method (FEM) is considered as the most thorough computational tool which provides the most detailed insight into the vehicle crash analysis. However, this approach requires powerful computational hardware resources in order to produce exact results. Apart from the technical aspects of FEM approach (like hardware availability or time-consuming simulation), the biggest challenge is to correctly select material properties of a colliding vehicle and its surroundings [1, 2]. Therefore, there are observable trends to decompose complex mesh models into arrangements which are less composite [3–7]. FEM model is capable of representing geometry and material details of a structure. The drawback of this method is the fact that it is costly (software and required hardware) and time-consuming. Additionally, the cost and time of such simulation is increased by the extensive representation of the major mechanisms in the crash event. When using FEM models, it is desirable to compare their results with the full-scale experimental measurements in order to enhance the simulation outcome. Decomposition of a complicated mesh model of a car into less complex arrangements also produces satisfactory results.

The secondary approach frequently utilized in vehicle crash modeling is lumped parameter modeling of viscoelastic systems [8–16]. Structural parameters of models like damping or stiffness are estimated based on a given crash scenario. The drawback of this method is that the obtained models cannot be used to simulate different crash scenarios and are valid only

W. Pawlus · H. R. Karimi (✉) · K. G. Robbersmyr
Department of Engineering, Faculty of Engineering and Science, University of Agder, PO BOX 509, 4898 Grimstad, Norway
e-mail: hamid.r.karimi@uia.no

W. Pawlus
e-mail: witold.pawlus@uia.no

K. G. Robbersmyr
e-mail: kjell.g.robbersmyr@uia.no

Published online: 06 October 2013

for one given set of collision conditions. Therefore, in [17, 18], there are proposed the efficient and reliable tools to assess structural parameters of a vehicle involved in various crash scenarios. In addition, the nonlinear models obtained in the literature consider the dynamic nature of a vehicle crash event and complexity of joints and interactions between particular car body's elements which results in the increased model's fidelity.

On the other hand, a field of research which is related to the methodology elaborated in this work is data-based modeling [19]. There have been numerous examples of applications of the autoregressive models like nonlinear autoregressive (NAR), nonlinear autoregressive with exogenous input (NARX), or nonlinear autoregressive moving average with exogenous input (NARMAX) to predict the time series data. It was shown that feedforward neural networks are special cases of autoregressive models, abbreviated NAR [20]. By following the same concept, it was found in [21], that the Bayesian framework can be successfully extended to multilayer perceptron, i.e., a feedforward network with the backpropagation teaching algorithm. Thanks to that operation, it was possible to compute the confidence limits for the prediction. Similarly to those two works, in [22], the parameters of ARX and NARX models were estimated using the feedforward neural networks. Different types of activation functions have been used and their effects on the network's overall performance have been evaluated. Bayesian network was successfully applied to recognize driver fatigue recognition as well [23]. Since aforementioned neural networks have high capabilities for the signals prediction purposes, they are commonly used, e.g., in machine diagnostics and failure detection. In [24], a hybrid of NARX and autoregressive moving average (ARMA) models was employed to forecast long-term machine state based on vibration data. The results have proven that such a model is a useful tool in the machine diagnostics and predicts well the degeneration index of a machine. The wide range of applications of this methodology is confirmed in [25]. Edge-localized modes time series analysis based on ARMA model has been successfully performed—it decomposed the time series into deterministic and noise components. NARX models have been successfully applied to black box modeling of the gas turbine operating in isolated and nonisolated mode too [26]. The variety of input signals (from narrow to broadband) were taken into account in the identification and validation stages of the modeling. Recurrent NARX models were formulated in [27]. The effects of the changing network's architecture on the quality of predictions were verified. Apart from the strictly engineering and technical applications of the regressive models, there is a huge number of works taking advantage of this methodology but devoted to the other areas of research. In [28, 29], one can find regressive models utilized, e.g., to forecast the stock market data—i.e., the weekly averaged exchange rates between the British pound and the US dollar in the given time period. A significant contribution was made in [30]. ARMA model was used to estimate lumped parameters (stiffness, damping, and mass) of analytical models (differential equations). Those physical parameters were changeable in time—thanks to that nonlinear model's behavior it was possible to simulate vehicle frontal and side impacts with high level of accuracy. The other efficient method—particle swarm optimization—was applied in [31]. It has a strong potential for models parameters estimation.

Up-to-date technologies are currently being utilized in the area of vehicle crash modeling—in [17, 32, 33], the results of application of wavelets and regressive approach to model a crash event are discussed. RBF neural networks have strong potential in modeling nonlinear time series data [34, 35]. Artificial neural networks (ANNs) are capable of not only reproducing car's kinematics but can be successfully applied to, e.g., predict the average speed on highways as it is shown in [36]. Training of the network was based on the data gathered by the radar gun and inputs consisted of geometric parameters (e.g., length of curve) and traffic parameters as well (e.g., annual daily traffic). On the other hand, ANNs were employed to predict injury severity of an occupant by less direct measurements too—using statistical data. Reference [37] presents a method for crash severity assessment based on the number of such inputs, like, e.g., driver age, alcohol use, seat belt use, vehicle type, time of the crash, light condition, or weather condition. Fuzzy logic together with neural networks and image processing has been employed in [38] to estimate the total deformation energy released during a collision. A vision system has been developed to record a crash event and determine relevant edges and corners of a car undergoing the deformation. Also, human action recognition was investigated in [39] by application of real-time video streams. In the most up-to-date scope of research concerning crashworthiness, it aims to define a dynamic vehicle crash model which parameters will be changing according to the changeable input (e.g., initial impact velocity). One of such trials is presented in [40]—a nonlinear occupant model is established, and scheduling variable is defined to formulate LPV (linear parameter varying) model. In [41–43], there are covered important aspects of signal processing and time series data preparation for proper analysis and identification.

There is a limited number of publications related to application of wavelet transform to vehicle crash modeling. One of such examples is [32]—the crash pulse recorded during a vehicle collision with a safety barrier was reproduced using Haar wavelet analysis. A similar reasoning is proposed in [44]. Decomposed crash signals are used to represent automobile vibrations occurring in certain time spans, which in turn are used to refine and validate a finite element vehicle crash model. Application of wavelets for validation of an FE model is covered in [45]. Since wavelet transform is a part of the multiresolution analysis, it gives a full insight into the time frequency character of a signal. For this reason, this approach

is widely utilized in diagnostics of structures, constructions, and devices [46–50]. Wavelet-based methods also find applications, e.g., in control algorithms for autonomous vehicles [51], pattern recognition and texture classification [52], or automatic incident detection on freeways which is an important component of an Advanced Traffic Management and Information Systems [53]. Also, decision support systems are used to authenticate the liability of traffic crashes [54].

The rest of the paper has been divided into the following parts. Section 2 describes the real crash test and presents the basic information regarding the instrumentation and measurements in this type of experiments. Layout of the experimental setup, type of vehicle, and obstacle or data acquisition process are some of the aspects which are thoroughly analyzed there. Section 3 is devoted to viscoelastic modeling of vehicle collisions. Principles needed to create spring–mass–damper models (in total, four different configurations) are presented and performance of each system discussed is assessed. Moreover, Section 4 contains the specification of a virtual crash test which was conducted to provide the authors with an additional dataset used in further part of the paper to increase the model's reliability and analyze the results more deeply. Mathematical derivation of the NAR model and artificial neural network is done in Section 5. Furthermore, in Section 5, subsequent steps needed to be followed to create a NAR model and feedforward neural network are described. It also includes the elaboration of network's structure and examination of its performance. Finally, the simulation results are presented. In Section 6, a detailed analysis and overview of the continuous wavelet transform are presented. Particular attention is paid to complex Morlet wavelet, as this is the wavelet elementary function which is used further in this work. A procedure for signal reconstruction based on wavelet transform is also described. On top of that, the discussed methods are applied to the measured vehicle crash acceleration signal. The crash pulse is decomposed into the components which have the greatest influence on its overall shape. The scale gram of the recorded crash pulse is calculated and its frequency–time relationship is observed. Subsequently, the major frequency constituents of the analyzed signal are identified. Finally, the acceleration signal is reconstructed from the skeletons of the ridges of the wavelet coefficients matrix for the major frequency components. Comparative analysis between the estimated vehicle kinematics and the reference one is presented at the end. Moreover, in Section 7, the results obtained in this work are compared with each other. It is also concluded on the benefits and limitations of each of the presented modeling methodologies. On top of that, suggestions for future activities are made.

The major contributions of the current study lie in exploring three vehicle crash modeling techniques and comparing their outcomes. Advantages and drawbacks of each method are briefly characterized. It is explained which approach, among the ones used in this work, is the most beneficial for modeling and simulation of a vehicle-localized impact. Another important contribution is that the simulation results are compared with a full-scale vehicle crash measurements, which greatly increases fidelity of the proposed models and validates usefulness of the discussed modeling techniques. As already mentioned in this section, the main motivation for this research is to enhance vehicle dynamics simulation, crash reconstruction, and prediction by using modeling strategies which allows making a quick assessment of vehicle structural parameters in an early design and development phase.

2 Experimental setup description

Since for each of the presented vehicle crash modeling methodologies, the same set of measurements from a full-scale collision is used, it was decided to characterize this vehicle crash test firstly. Experimental setup description is covered in details in [55]. It is a typical midspeed vehicle-to-pole collision scheme showing the layout of the test setup is illustrated in Fig. 1.

The vehicle has an initial velocity of 35 km/h while impacting the obstacle. Its total mass including the measuring equipment and dummy was determined to be 873 kg. During the test, the acceleration at the center of gravity (COG) in three dimensions (x-longitudinal, y-lateral, and z-vertical) was recorded. The yaw rate was also measured with a gyro meter.

2.1 Vehicle center of gravity determination procedure

To properly mount an accelerometer, it was necessary to correctly determine a vehicle's COG. It was achieved by weighting the vehicle in a horizontal position using four load cells. Afterwards, the vehicle was tilted by lifting its frontal part. The following notation is used:

- m_1 wheel load, front left (in kilograms)
- m_2 wheel load, front right (in kilograms)
- m_3 wheel load, rear left (in kilograms)
- m_4 wheel load, rear left (in kilograms)
- m_v total load (without data acquisition system nor dummy) (in kilograms)
- m_f front mass in tilted position (in kilograms)
- m_b rear mass in tilted position (in kilograms)
- Θ angle of tilt (in degrees)
- l wheel base (in meters)
- d distance across the median plane between the vertical slings from the lift brackets at the wheel centers and the load cells (in meters)

The above procedure is illustrated in Figs. 2 and 3, whereas the numerical values obtained are summarized in Table 1. The following formulas were used to determine location of vehicle's center of gravity:

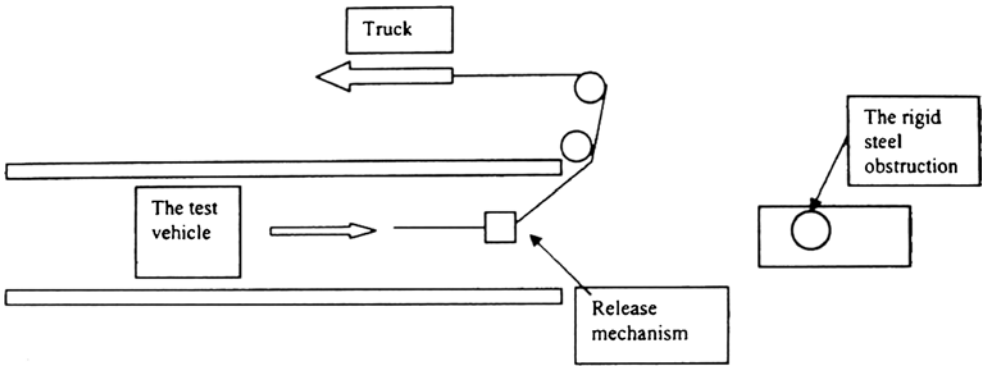

Fig. 1 Scheme of the experiment

1. Longitudinal location—the horizontal distance between COG and the front axle centerline:

$$\mathrm{COG}_x = \frac{m_3 + m_4}{m_v} \cdot l \tag{1}$$

2. Lateral location—the horizontal distance between the longitudinal median plane of the vehicle and COG:

$$\mathrm{COG}_y = \frac{m_1 + m_3 - (m_2 + m_4)}{m_v} \cdot \frac{d}{2} \tag{2}$$

3. Vertical location—COG location above a plane through the wheel centers:

$$\mathrm{COG}_z = \frac{(m_1 + m_2 - m_f) \cdot l}{m_v \cdot \tan\Theta} \tag{3}$$

The location of COG is determined to be:

1. COG_x=0.87 (in meters)
2. COG_y=0.03 (in meters)
3. COG_z=0.26 (in meters)

2.2 Vehicle and obstacle

The dimensions of the car are shown in Fig. 4 and listed in Table 2. The obstruction and car themselves are shown in Figs. 5 and 6, respectively. Using normal- and high-speed video cameras (recording rate was 250 frames per second), the behavior of the test vehicle during the collision was recorded (see Fig. 7).

2.3 Data acquisition

The acceleration was recorded by using sa 3D accelerometer. The accelerometer was a piezoresistive triaxial sensor with a range of ±1,500 g. This device was mounted on a steel bracket in the vehicle's center of gravity and the bracket was fastened by screws to the vehicle's chassis. The yaw rate was measured with a gyro instrument which makes it is possible to record 1°/s. Data from the sensor was fed to an eight-channel data logger and sampled with a frequency of 10 kHz. The velocity of the vehicle was checked by an inductive monitor. It was directed towards a perforated disc mounted on a wheel on the right side of the test vehicle (see Fig. 8). Video recorders arrangement is presented in Fig. 9.

2.4 Real crash pulse analysis

Having at our disposal the acceleration measurements from the collision, we are able to describe in details the motion of the car. Since it is a central impact, we analyze only the pulse recorded in the longitudinal direction (x-axis). By integrating car's deceleration, we obtain plots of velocity and displacement, respectively (see Fig. 10). At the time when the relative approach velocity is zero (t_m), the maximum dynamic crush (d_c) occurs. The relative velocity in the rebound phase then increases negatively up to the final separation (or rebound) velocity, at which time a vehicle rebounds from an obstacle. The contact duration of the two masses includes both contact times in deformation and restitution phases. When the relative acceleration becomes zero and relative separation velocity reaches its maximum recoverable value, we have the separation of the two masses. From the crash pulse analysis, we obtain the data listed in Table 3.

Fig. 2 Vehicle weighted in horizontal position

Fig. 3 Vehicle weighted in titled position

3 Lumped parameter models

In this approach, we present the methodology to create viscoelastic models of vehicle crash according to [14]. We start with simulation of the vehicle to pole impact by using the simple mass–spring model, and then we extend the analysis to so-called Kelvin model (spring and damper in parallel connected to mass). Afterwards, the system in which spring and damper are connected in series (so called Maxwell model) is examined and it is being assessed which of them gives the most exact description of the car's behavior in the pole collision.

3.1 Spring–mass model

The motion of this system is a nondecayed oscillatory one (sinusoidal) because there is no damping in it [56]. This arrangement is shown in Fig. 11; symbols—k, spring stiffness; m mass; a, absolute displacement of mass m.

Let us introduce the following notation:

V initial barrier impact velocity (in meters per second)
f structural natural frequency (in Hertz)

The response of this system is characterized by the following equations:

Table 1 Data for determination of vehicle center of gravity

Parameter	Value
m_1 (kg)	257
m_2 (kg)	237
m_3 (kg)	154
m_4 (kg)	150
m_v (kg)	798
m_f (kg)	444
m_b (kg)	354
d (m)	1.73
l (m)	2.28
Θ (degree)	28.4

$$\ddot{\alpha}(t) = -V\omega_e \sin(\omega_e t) \tag{4}$$

$$\dot{\alpha}(t) = V\cos(\omega_e t) \tag{5}$$

$$\alpha(t) = \frac{V}{\omega_e}\sin(\omega_e t) \tag{6}$$

which represent deceleration, velocity, and displacement, respectively. Furthermore, we define:

$$C = \frac{V}{\omega_e} \tag{7}$$

$$t_m = \frac{\pi}{2\omega_e} \tag{8}$$

$$\omega_e = \sqrt{\frac{k}{m}} \tag{9}$$

as maximum dynamic crush, time of maximum dynamic crush, and system's circular natural frequency, respectively.

To investigate what the parameters C and t_m of such a model are; first, we need to find the spring stiffness k. By substituting (9) to (7) and rearranging, one gets:

$$k = \frac{V^2}{C^2}m \tag{10}$$

From Fig. 10, C=0.52 m= 52 cm and V=9.86 m/s= 35 km/h is obtained. Therefore:

$$k = \frac{(9.86\,\mathrm{m/s})^2}{(0.52)^2}873\,\mathrm{kg} = 313,878\,\mathrm{N/m}$$

$$t_m = \frac{\pi}{2\omega_e} = \frac{\pi}{2\sqrt{\frac{k}{m}}} = \frac{\pi}{2\sqrt{\frac{313,878\,\mathrm{N/m}}{873\,\mathrm{kg}}}} = 0.083\mathrm{s}$$

Spring–mass model's response for above spring stiffness k (initial velocity and mass of the car remain the same) is shown in Fig. 12. Let us compare what the dynamic crush and the time at which it occurs are for the car and model (see Table 4).

Results obtained in this step are good. The dynamic crush estimated by the spring–mass model is exactly the same as the reference dynamic crush of a real car. Regarding the time when it occurs, the difference between the model and reality is less than 1 %. This model gives good approximation of the car's behavior during the crash. It is a particular case of a Kelvin model in which damping has been set to zero as well as of a Maxwell model in which damping goes to infinity.

3.2 Kelvin model

The Kelvin model shown in Fig. 13 has been proposed to represent the vehicle to pole collision. Symbols used—k,

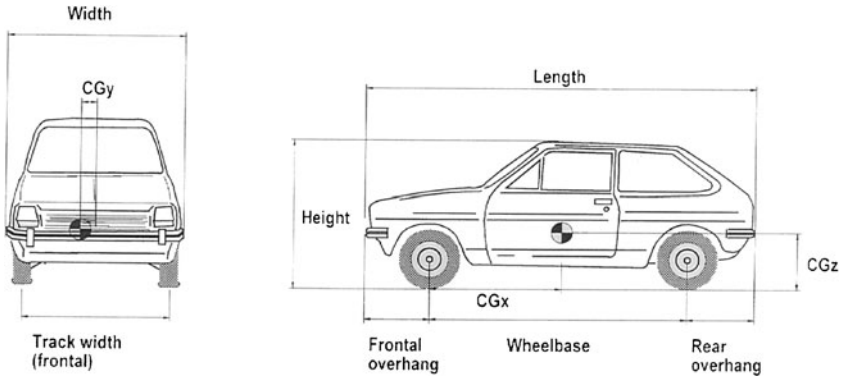

Fig. 4 Car used in the crash test

spring stiffness; c, damping coefficient; m, mass; and V_0, initial impact velocity.

Transient responses of the underdamped Kelvin model are given by the following formulas (displacement, velocity, and acceleration, respectively):

$$\alpha(t) = \frac{v_0 e^{-\zeta\omega_e t}}{\sqrt{1-\zeta^2}\omega_e} \sin\left(\sqrt{1-\zeta^2}\omega_e t\right) \tag{11}$$

$$\dot{\alpha}(t) = v_0 e^{-\zeta\omega_e t}\left[\cos\left(\sqrt{1-\zeta^2}\omega_e t\right) - \frac{\zeta}{\sqrt{1-\zeta^2}} \sin\left(\sqrt{1-\zeta^2}\omega_e t\right)\right] \tag{12}$$

$$\ddot{\alpha}(t) = v_0\omega_e e^{-\zeta\omega_e t}\left[-2\zeta\cos\left(\sqrt{1-\zeta^2}\omega_e t\right) + \frac{2\zeta^2-1}{\sqrt{1-\zeta^2}} \sin\left(\sqrt{1-\zeta^2}\omega_e t\right)\right] \tag{13}$$

where: $\zeta = \frac{c}{2m\omega_e}$ and $\omega_e = \sqrt{\frac{k}{m}}$.

By following the method developed in [56], we calculate Kelvin model's coefficients. Known parameters are:

m=873 kg mass of the car
v_0=9.86 m/s initial impact velocity

The parameters which we obtain from the crash pulse analysis are illustrated in Fig. 10. We calculate the centroid time:

Table 2 Major car's dimensions

Dimension	Value (m)
Width	1.58
Length	3.64
Height	1.39
Wheel base	2.28
Frontal overhang	0.66
Rear overhang	0.70
Wheel track: front axle	1.38
Wheel track: rear axle	1.34

$$t_c = \frac{C}{v_0} = \frac{0.52\,\text{m}}{9.86\,\text{m/s}} = 0.053\,\text{s} \tag{14}$$

and relative centroid time:

$$\frac{t_c}{t_m} = \frac{0.053s}{0.076s} = 0.7 = \frac{\sqrt{1-\zeta^2}}{\arctan\frac{\sqrt{1-\zeta^2}}{\zeta}} e^{\left[\frac{-\zeta}{\sqrt{1-\zeta^2}}\arctan\frac{\sqrt{1-\zeta^2}}{\zeta}\right]} \tag{15}$$

By taking advantage of (15), we find the value of damping coefficient ζ=0.05. Having ζ, from (16), we determine value of ft_m=0.24.

$$ft_m = \frac{1}{2\pi\sqrt{1-\zeta^2}} \arctan\frac{\sqrt{1-\zeta^2}}{\zeta} \tag{16}$$

Structure natural frequency is then equal to:

$$f = \frac{0.24\,\text{Hz·s}}{0.076\,\text{s}} = 3.1616\,\text{Hz} \tag{17}$$

Spring stiffness k and damping coefficient c of the Kelvin model are determined to be:

$$k = 4\pi^2 f^2 \text{m} = 344,150\,\text{N/m} \tag{18}$$

$$c = 4\pi f\zeta m = 1,733\,\text{Ns/m} \tag{19}$$

Fig. 5 Obstruction

Fig. 6 Car's deformation

Fig. 8 Velocity verification device

Kelvin model response for those parameters is shown in Fig. 14. Comparison between the model and reality for the filtered data is done in Table 5.

We observe a larger discrepancy between the dynamic crush from the acceleration's integration and model's prediction than for the spring–mass model. This allows us to claim that since the method of parameters estimation utilized in both of those cases is based on a similar approach, the Kelvin model is not suitable for modeling the impact examined by us. For that reason, we investigate a model which consists of spring and damper connected in series to a mass.

3.3 Maxwell model—introduction

The arrangement in which spring and damper are connected in series to mass is called Maxwell model (Fig. 15). To derive its equation of motion, it is proposed to place small mass m' between spring and damper. By doing this, the inertia effect which occurs for the spring and damper is neglected and the system becomes third order differential equation which can be solved explicitly [56]. According to Fig. 15, we define d and d' as absolute displacement of mass m and absolute displacement of mass m', respectively. We establish the following equations of motion (EOM):

$$m\ddot{d} = -c(\dot{d} - \dot{d'}) \tag{20}$$

$$m'\ddot{d'} = c(\dot{d} - \dot{d'}) - kd' \tag{21}$$

By differentiating (20) and (21) w.r.t. time and setting $m'=0$ we obtain:

$$m\dddot{d} = -c\left(\ddot{d} - \ddot{d'}\right) \tag{22}$$

$$0 = c\left(\ddot{d} - \ddot{d'}\right) - k\dot{d'} \tag{23}$$

We sum up both sides of (22) and (23) and rearrange:

$$\dot{d'} = \frac{-m}{k}\dddot{d} \tag{24}$$

We substitute (24) into (20) and finally obtain the undermentioned EOM:

$$\dddot{d} + \frac{k}{c}\ddot{d} + \frac{k}{m}\dot{d} = 0 \tag{25}$$

Fig. 7 Subsequent steps of the crash test

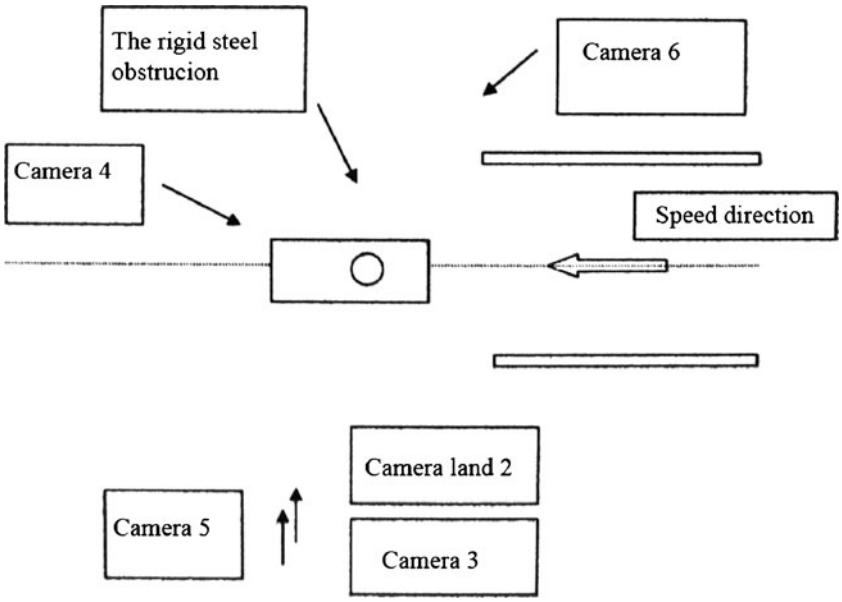

Fig. 9 Visual data acquisition system layout

Therefore, characteristic equation of the Maxwell model is:

$$s\left[s^2+\frac{k}{c}s+\frac{k}{m}\right]=0 \tag{26}$$

In this system, the rebound of the mass depends on the sign of discriminant Δ of the quadratic equation in brackets. For positive Δ, there is no rebound, i.e.,:

$$\left(\frac{k}{c}\right)^2 > 4\frac{k}{m}$$

In this case, roots of the characteristic Eq. (26) are respectively:

$$s_0 = 0$$
$$s_1 = a+b$$
$$s_2 = a-b$$

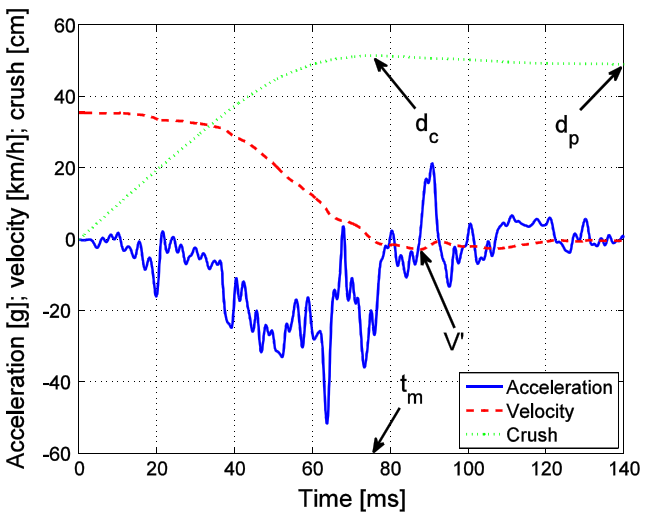

Fig. 10 Vehicle kinematics

where:

$$a = \frac{-k}{2c}$$
$$b = \sqrt{\left(\left(\frac{k}{2c}\right)^2-\frac{k}{m}\right)}$$

On the other hand, for negative Δ, the rebound occurs when:

$$\left(\frac{k}{c}\right)^2 < 4\frac{k}{m}$$

In this case, roots of the characteristic Eq. (26) are, respectively:

$$s_0 = 0$$
$$s_1 = a+ib$$
$$s_2 = a-ib$$

Table 3 Parameters characterizing the real crash pulse

Parameter	Value
Initial impact velocity, V (km/h)	35
Rebound velocity, V' (km/h)	3
Maximum dynamic crush, d_c (cm)	52
Time when it occurs t_m (ms)	76
Permanent deformation d_p (cm)	50

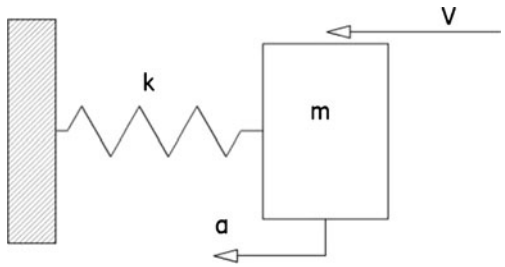

Fig. 11 Spring-mass model

where:

$$a = \frac{-k}{2c}$$

$$b = \sqrt{\left(\frac{k}{m} - \left(\frac{k}{2c}\right)^2\right)}$$

Since this case is of our greater interest than the previous one (due to the fact that in the experiment rebound occurred), we will describe in details its response. Displacement of a mass is given by the formula:

$$\alpha = d_0 e^{s_0 t} + e^{at}[d_1 \sin(bt) + d_2 \cos(bt)] \tag{27}$$

Initial conditions (t= 0) are:

$$\alpha = 0$$
$$\dot{\alpha} = v$$
$$\ddot{\alpha} = 0$$

Where v is the initial impact velocity. Constants are:

$$d_2 = \frac{2av}{a^2 + b^2}$$
$$d_1 = \frac{v - ad_2}{b}$$
$$d_0 = -d_2$$

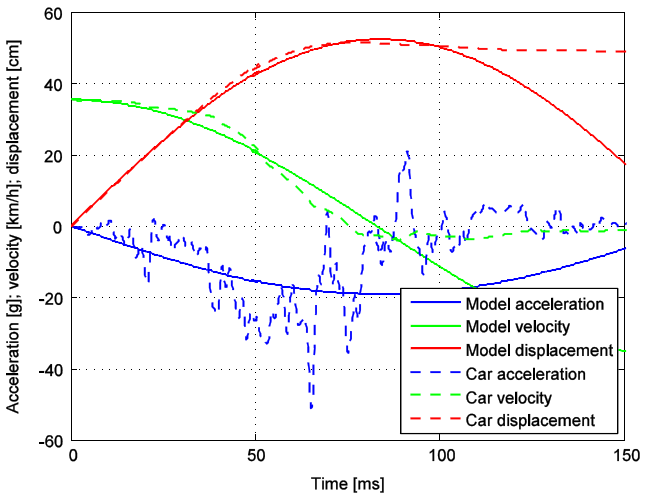

Fig. 12 Spring-mass model response

Table 4 Comparison between car and spring–mass model responses

Parameter	Crash pulse analysis	Spring-mass model
Dynamic crush, d_c (cm)	52	52
Time of dynamic crush, t_m (ms)	76	83

However, in a Maxwell model, the mass may not rebound from the obstacle. It means that its displacement increases with time to an asymptotic value. The parameter, which determines whether the rebound will occur or not, is damping coefficient. When it is less than a limiting one (named transition damping coefficient c^*), the mass will be constantly approaching an obstacle, whereas when it is higher, there will exist a dynamic crush at a finite time. Another boundary situation is for damping coefficient $c = \infty$. Then the Maxwell model degenerates into spring–mass system. To determine the value of transition damping coefficient we assume that $c = 0$, or equivalently

$$\frac{k}{c^*} = 2\sqrt{\frac{k}{m}}$$

and

$$c^* = \frac{\sqrt{km}}{2} \tag{28}$$

Indeed, for $c < c^*$, we have $\Delta > 0$—it means no dynamic crush at a finite time.

We are able to assess what the minimal damping should be, which we add to the simple spring–mass model mentioned above, which will produce the dynamic crush not extended in an infinite period of time. According to (28), for the model and crash test being analyzed in Section 3.1, we calculate the transition damping coefficient:

$$c^* = \frac{\sqrt{313,878\,\mathrm{N/m} \cdot 873\ \mathrm{kg}}}{2} = 8,277\,\mathrm{N \cdot s/m}$$

For every damping greater than this value, the Maxwell model formed from the spring–mass model from Section 3.1, will give us the response more and more similar to the spring–mass model characteristics presented in Fig. 12, as it is shown in Fig. 16.

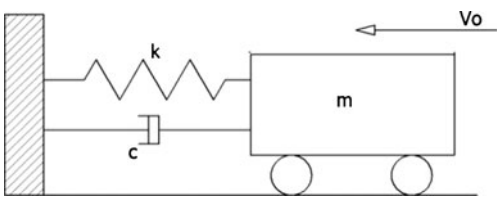

Fig. 13 Kelvin model

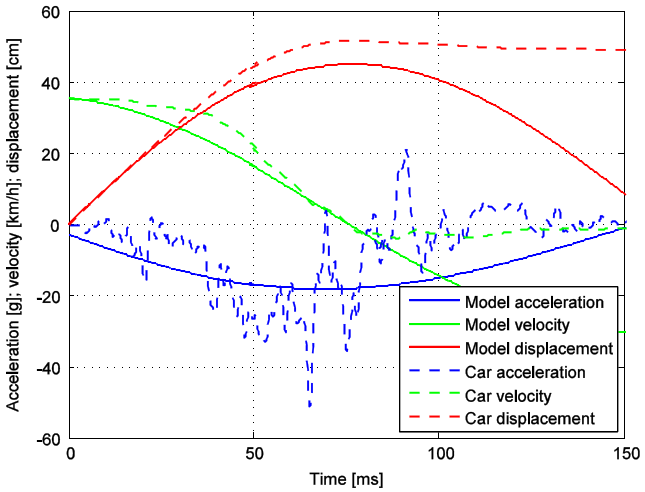

Fig. 14 Kelvin model response

It is noted that the final displacement (or asymptotic value—for transition damping coefficient) achieved by the mass in this model is characterized by the equation (V_0, initial impact velocity; m, mass; c, damping coefficient):

$$\text{crush} = \frac{V_0 m}{c} \tag{29}$$

This system is appropriate for simulating soft impacts or offset impacts because the time of dynamic crush is longer than for Kelvin model. We assume the same parameters for both models, e.g.,:

$$k = 100\ \text{N/m}, c = 15\ N\text{–s/m}, m = 5\ \text{kg}, v_0 = 10\ \text{m/s}.$$

In Fig. 17, it is seen that for the Maxwell model, the dynamic crush occurs later than for the Kelvin model.

This is an analog situation to the real crash: in a vehicle-to-rigid barrier collision (Kelvin model), the whole impact energy is being consumed faster; therefore, the crash is more dynamic than the vehicle-to-pole collision (Maxwell model)—under the assumption that we compare the same cars with the same initial impact velocities—as in the example above. It is noting that we do not investigate here the magnitude of the displacement of both models—as we can see for the same parameters, it is higher for the Maxwell model. The above example just illustrates the dynamic responses of those two systems and in order to apply those two models to the real crash, one need to assess what spring stiffness and damping coefficient of both of them are separately.

Table 5 Comparison between car and Kelvin model responses

Parameter	Crash pulse analysis	Kelvin model
Dynamic crush, d_c (cm)	52	43
Time of dynamic crush, t_m (ms)	76	83

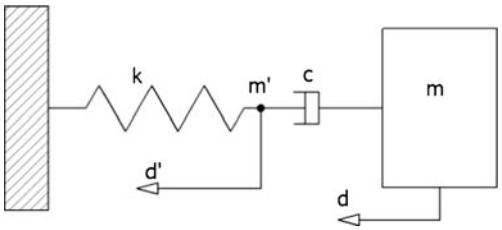

Fig. 15 Maxwell model (m') designates zero mass

3.4 Maxwell model creation

Only two examples of Maxwell model are discussed for which $\Delta < 0$, i.e., when the rebound occurs, because that is what happens during the experiment. We are going to start with the simplification of this situation, in which damping coefficient of this model has a limiting, transitional value. Then, we proceed to the full Maxwell model's analysis.

Maxwell model with transition damping coefficient is the particular case of a Maxwell model in which mass displacement reaches an asymptotic value given by (29). For

$$c^* = \frac{\sqrt{km}}{2}$$

parameters of (27) degenerate into:

$$\begin{aligned} a &= -\omega \\ b &= 0 \\ d_1 &= -\frac{v}{b} \\ d_2 &= -2\frac{v}{\omega} \\ d_0 &= 2\frac{v}{\omega} \end{aligned}$$

where

$$\omega = \sqrt{\frac{k}{m}}$$

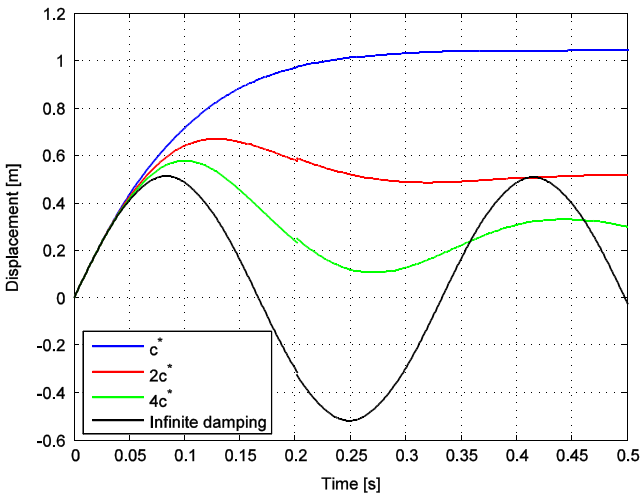

Fig. 16 Maxwell model responses for different values of damping

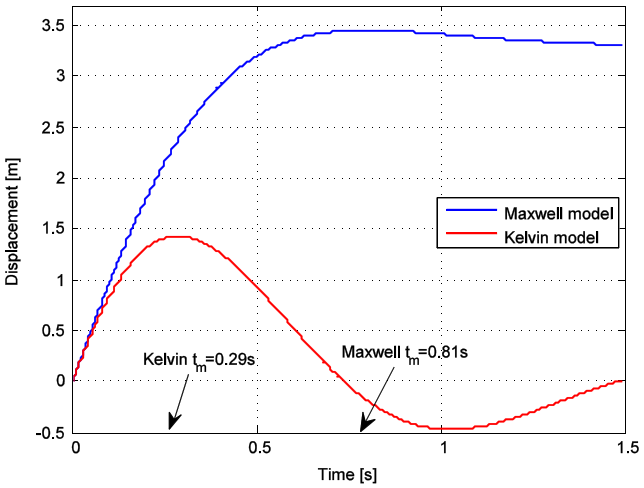

Fig. 17 Maxwell and Kelvin models responses comparison

We take advantage of trigonometric relationships:

$$\lim_{b\to 0}\frac{\sin(bt)}{b} = t$$
$$\lim_{b\to 0}\cos(bt) = 1$$

Finally, we come up with the following equation of mass displacement:

$$\alpha = \frac{v}{\omega}\left[2-(\omega t+2)e^{-\omega t}\right] \tag{30}$$

To establish the parameters of the Maxwell model (spring stiffness k and damping coefficient c), we just substitute to (30) values of v, α, and t_m taken from the acceleration measurements analysis shown in Fig. 10—we obtain ω= 37.52 rad/s. Knowing circular natural frequency ω and mass of the whole vehicle m=873 kg, we calculate spring stiffness k and transition damping coefficient c^*:

$$k = \omega^2 \mathrm{m} = 37.24^2 \cdot 873 = 1,228,966\ \mathrm{N/m}$$
$$c^* = \frac{\sqrt{km}}{2} = \frac{\sqrt{1,228,966\cdot 873}}{2} = 16,377\ \mathrm{N\cdot s/m}$$

Response of the model with above computed parameters and initial impact velocity v=9.86 m/s=35 km/h is shown in Fig. 18.

As we can see, the value of maximum dynamic crush is the same as the one obtained from the experiment's data analysis (C=0.52 m) and time when it occurs is much longer—approximately t_m=0.2 s (compared to experimental t_m= 0.076 s;).

The response of the Maxwell model is described by (27). Having the car's displacement curve from the experiment, we can establish parameters of the model (spring stiffness k and damping coefficient c) just by fitting the curve defined by (27) to that real graph. However, parameters which we obtain by fitting (27) are a, b, d_0, d_1, and d_2. Since d_1 and d_2 (we do not discuss d_0 separately because $d_0=-d_2$) are functions of v as well, it is not guaranteed that the model's parameters which we obtained would be correct—in another words, v would not be fixed if we fit (27) to the experiment's displacement. Therefore, we express (27) only in terms of a and b (which are just functions of k, c and mass m=873 kg) and set initial impact velocity to v=9.86 m/s. The equation which we obtain has the following form:

$$\alpha = -\frac{2av}{a^2+b^2} + e^{at}\left[v - \frac{2a^2v}{a^2+b^2}\frac{\sin(bt)}{b} + \frac{2av}{a^2+b^2}\cos(bt)\right] \tag{31}$$

Fitting (31) to the experiment's results has been done in Matlab Curve Fitting Toolbox and is shown in Fig. 19. Fitting (31) not (27) resulted in loss of approximation's accuracy but on the other hand, we are sure that the initial impact velocity has the correct value. From the above operation, we obtain parameters a and b of (31) which are equal to:

$$a = \frac{-k}{2c} = -14.79\frac{1}{s}$$
$$b = \sqrt{\left(\frac{k}{m}-\left(\frac{k}{2c}\right)^2\right)} = 21.06\frac{1}{s^2}$$

The damping coefficient c and spring stiffness k of the Maxwell model are determined to be, respectively:

$$c = \frac{m\left(a^2+b^2\right)}{-2a} = 19,546\,\mathrm{N\cdot s/m}$$
$$k = -2ac = 578,171\,\mathrm{N/m}$$

The response of the model is shown in Fig. 20. As we can see, the value of maximum dynamic crush is exactly the same as the one obtained from the experiment's data analysis (C=52 cm) and time when it occurs is longer—t_m=104 ms (compared to the experiment's t_m=76 ms). However, the overall response of the Maxwell model is similar to the car's behavior during collision with a pole.

3.5 Discussion

To represent vehicle-to-pole collision, four models were established (spring–mass model, Kelvin model, Maxwell model with transition damping coefficient, and complete Maxwell model). Characteristics which the best represents the overall car's behavior during the crash period belongs to the Maxwell model. Although Kelvin and spring–mass models give good approximation in the beginning of the crash

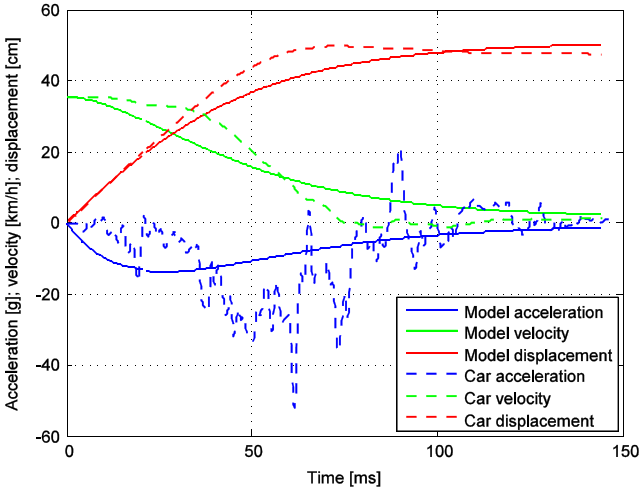

Fig. 18 Maxwell model (transition damping coefficient) response

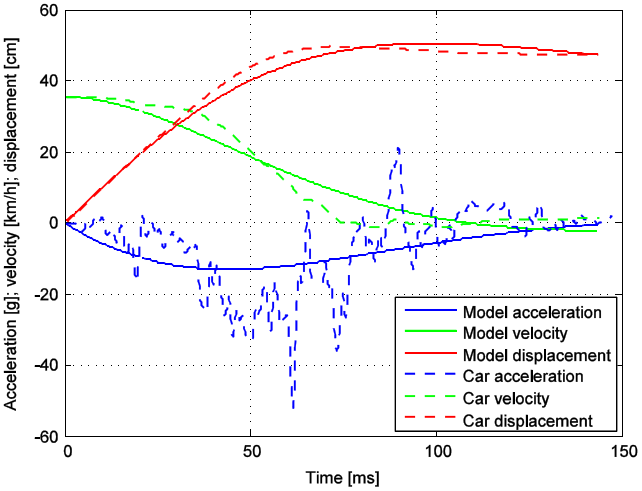

Fig. 20 Complete Maxwell model response

(up to the time of maximum dynamic crush), they completely fail to represent the crash after the rebound. Maxwell model with transition damping coefficient shows correctly just the maximum dynamic crush, not its time at all. Therefore, the Maxwell model gives the best overall outcome—there is no difference in maximum displacement and about 27 % of divergence for time of maximum dynamic crush compared to the reality. On top of that, the entire shape of the Maxwell model response resembles closely the real car's crush. These results directly correspond to findings explored in details in [56] regarding modeling of vehicle localized impacts.

4 Virtual crash test description

In order to generate new dataset which will be used further in the text to evaluate the proposed vehicle crash modeling methodology, it was decided to create a virtual crash test according to [19]. The virtual experiment has been performed

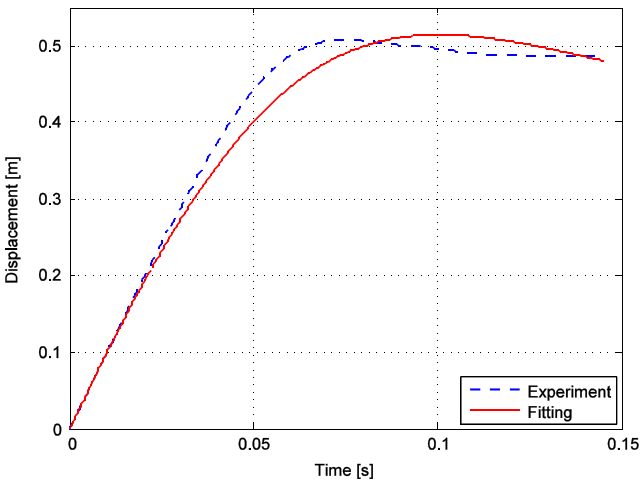

Fig. 19 Fitting the Maxwell model response to the real experiment's displacement

to provide another dataset to increase the number of simulated vehicle crash scenarios. This has been done to make the results more reliable. Also, adding new crash scenarios helped to strengthen the contributions of this work. To make the virtual experiment as reliable as possible, we have decided to reproduce one of the huge numbers of collisions presented in [56]. We have chosen on purpose a low-speed collision (22 km/h compared to 35 km/h from the real crash test presented in Section 2) and similar car's type as well as its dimensions to check if it is possible to establish a model applicable to two different collision types and two different initial impact velocities (however, to the similar car's type).

4.1 Methodology and assumptions

A multibody car model has been built. We have divided the front part of the vehicle into six undeformable components as we can assume that in such a type of collision only this car's section undergoes the deformation. To simulate elastoplastic properties of the car's body, its particular components were connected with springs and dampers (see Fig. 21). To make the vehicle follow the reference car's behavior from [56], their values were assigned in the trial and error method (see Table 6). Furthermore, since we investigate a central collision, the whole model is constrained in such a way that its motion is possible only in one direction—longitudinal. By doing this, we analyze only its longitudinal acceleration component—the same as it was done in Section 2 (Table 6).

4.2 Vehicle description

The most relevant dimensions of the car are shown in Figs. 22 and 23. They were assigned to fulfill the overall mid-size vehicle geometric requirements. Mass of the whole vehicle is equal to 1,000 kg. Mass distribution was also taken into account

(e.g., the front part of the hood is not heavy, on the other hand, the axle together with wheels and engine weigh more).

4.3 Virtual crash pulse analysis

Sampling rate for the virtual experiment is exactly the same as the one for the real collision elaborated in Section 2—i.e., 10 kHz (according to [57]). Similarly, the acceleration was measured in the car's center of gravity (COG, see Fig. 24)—subsequent steps of a virtual collision are illustrated in Fig. 25. In Fig. 26, there is shown virtual experiment's outcome. Keep in mind that the response obtained from the virtual crash test should be treated as the approximated crash pulse since it is not possible to get such rapidly changing acceleration plot (as it is in the real experiment) in this kind of simulation. However, the results are satisfactory because the obtained virtual car's deformation closely follows the reference one from [56], as well as the overall shapes of velocity and acceleration. See Table 7 for the most relevant crash pulse characteristic parameters. The value of permanent deformation (d_p) for the virtual experiment should be treated as the approximated one, since the whole model is represented as a multibody. As we see, the crush curve in Fig. 12 do not achieve a steady value. However, the behavior of this model in the crush time interval (up to the moment when the acceleration plot reaches the zero value) is satisfactory.

5 Data-based modeling by nonlinear autoregressive model and feedforward neural network

This work contains an analysis of a NAR model established for a full-scale crash test and virtual vehicle collision according to [19]. The main contribution of this research is that presented results are evaluated and compared with the original experimental measurements. Additionally, the performance of the created NAR model is verified by its application to reproduce the kinematics of a vehicle under different collision circumstances than the ones which occurred for the vehicle which crash test data was used to formulate it. To the knowledge of the authors, such application of NAR model to reconstruct vehicle collisions has not been discussed in the literature before. The originality of the presented method is directly related to exploring the field of vehicle dynamics modeling by using nonlinear autoregressive models.

5.1 NARMA model derivation

In [58], nonlinear autoregressive with moving average (NARMA) model parameters were obtained from three-layer neural network in which activation function was in form of a polynomial. Since NARMA model is a general case of NAR model, its derivation will be covered first to gain better understanding of the NAR model itself utilized by us. A nonlinear, time invariant, discrete time dynamic system can be successfully represented by the following NARMA model [58]:

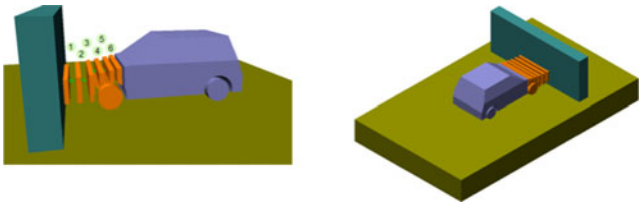

Fig. 21 Virtual experiment overview

$$
\begin{aligned}
y(n) = &\sum_{i=0}^{P} a(i)u(n-i) + \sum_{j=1}^{R} b(i)y(n-j) \\
&+ \sum_{i=0}^{P}\sum_{j=0}^{P} a(i,j)u(n-i)u(n-j) \\
&+ \sum_{i=1}^{R}\sum_{j=1}^{R} b(i,j)y(n-i)y(n-j) \\
&+ \sum_{i=0}^{P}\sum_{j=1}^{R} c(i,j)u(n-i)y(n-j) + \ldots + e(t)
\end{aligned} \tag{32}
$$

where P and R are orders of the moving average and autoregressive terms (both linear and nonlinear). In particular, $a(i)$ and $a(i, j)$ are the linear and nonlinear moving average terms; $b(i)$ and $b(i, j)$ are the linear and nonlinear ARMA terms; $c(i, j)$ are the nonlinear cross terms; $y(n)$ is the system output signal; $u(n)$ is the input signal; $e(n)$ is the error; and i, j, m, and n are indices. The output signal $y(n)$ from (32) may be expressed as:

$$
y(n) = \sum_{i=1}^{M} c_i p_i(x_i) + e(n) \tag{33}
$$

where $\{p_i(x_i)\}^{M}{}_{i=1}$ is a set of basic functions including past values of output $y(n)$ and present values and past values of input $u(n)$. The weight of the coupling of hidden unit i to the output unit is $c(i)$, the number of the hidden units is M, and

Table 6 Values of stiffness and damping for each spring

Spring number	Stiffness c (kN/m)	Damping k (kNs/m)
1	90	70
2	500	80
3	100	10
4	800	6
5	600	10
6	30	70

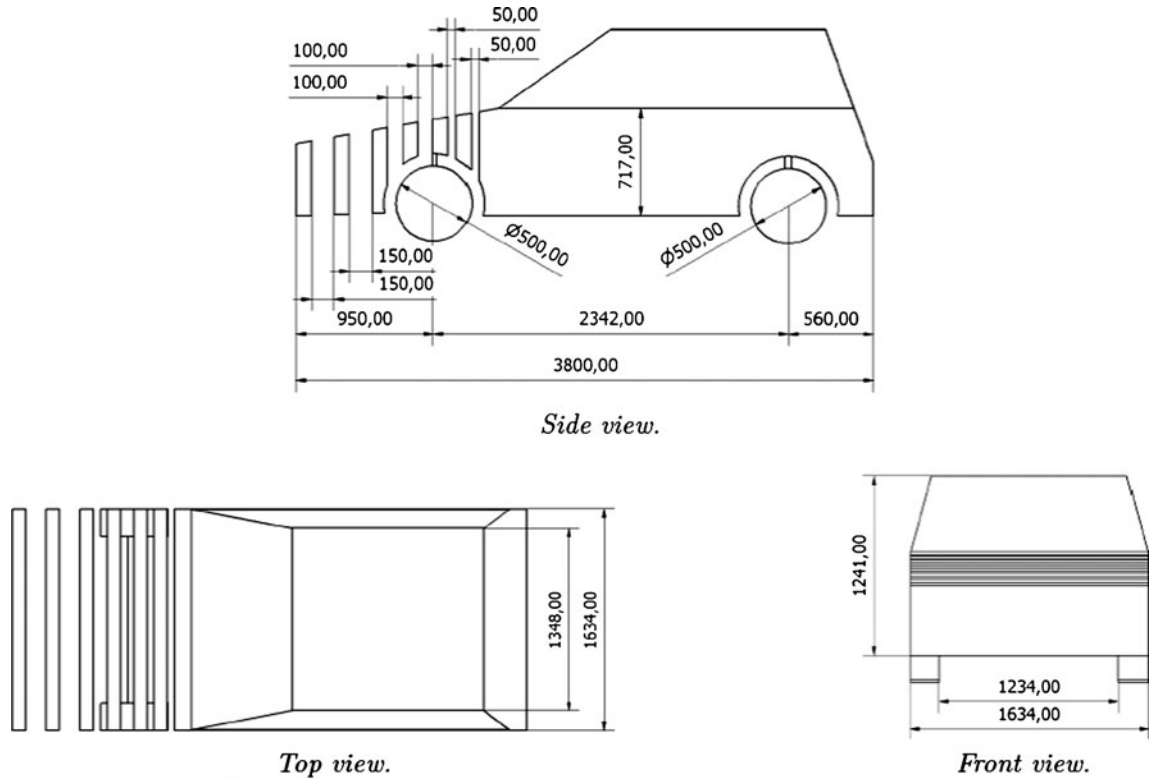

Fig. 22 Overall dimensions of the virtual vehicle given in millimeter

the weighted sum of inputs to the hidden unit i is x_i, expressed as:

$$x_i = \sum_{j=0}^{P} \omega_{ji} u(n-j) + \sum_{j=1}^{R} v_{ji} y(n-j) \tag{34}$$

According to [58], let us define the basis function from (33) as a polynomial function:

$$p_i(x) = a_{0i} + a_{1i}x + a_{2i}x^2 + \ldots + a_{ni}x^n + \ldots \tag{35}$$

By substituting (35) into (33), we obtain the following relationship describing the output:

$$\begin{aligned} y(n) = {} & c_1\left(a_{01} + a_{11}x_1 + a_{21}x_1^2 + \ldots\right) \\ & + c_2\left(a_{02} + a_{12}x_2 + a_{22}x_2^2 + \ldots\right) \\ & + c_M\left(a_{0M} + a_{1M}x_M + a_{2M}x_M^2 + \ldots\right) + e(n) \end{aligned} \tag{36}$$

By further substitutions (x_i from (34) into (36)), one can obtain an equivalent equation for (32), in which linear and

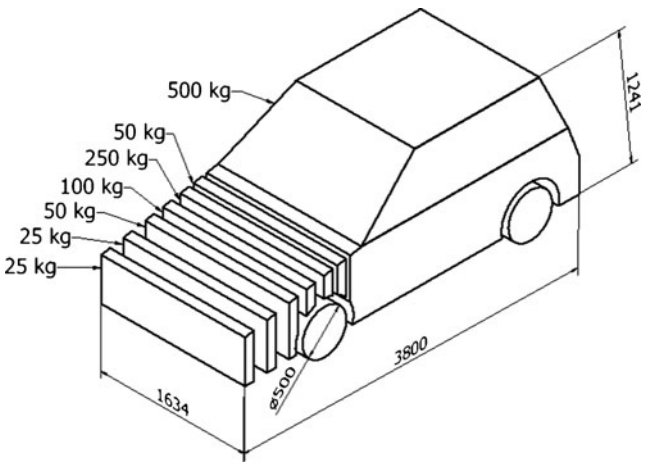

Fig. 23 3D model of a virtual vehicle—dimensions in millimeter

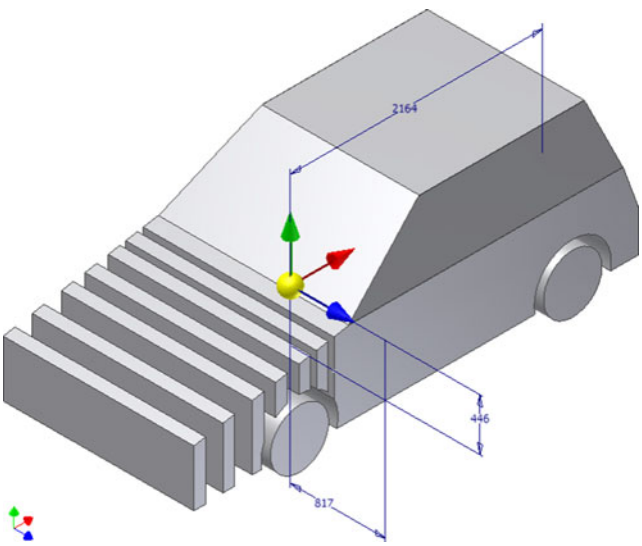

Fig. 24 Center of gravity (COG) of a virtual car

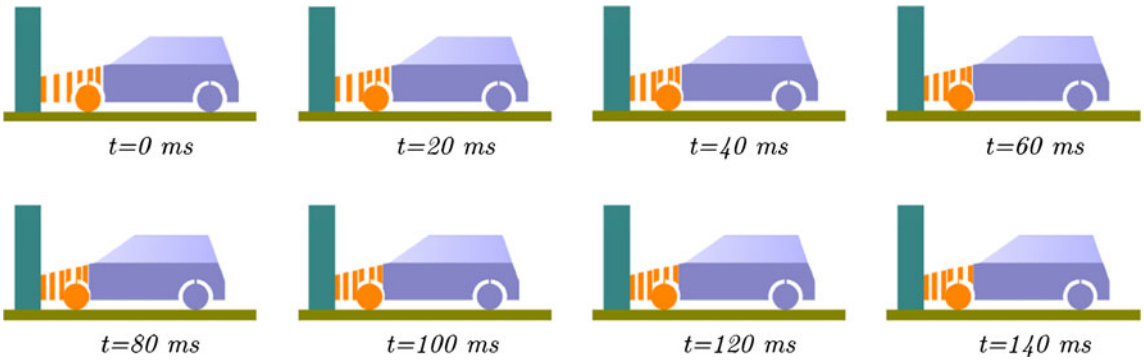

Fig. 25 Sequence of a simplified virtual crash test

nonlinear coefficients from (32) will be represented by neural network weight values and polynomial coefficients. Therefore, it is possible to get coefficients of the NARMA model by solving the following formulas:

$$a(i) = \sum_{s=1}^{M} c_s a_{1s} \omega_{is} \tag{37}$$

$$b(i) = \sum_{s=1}^{M} c_s a_{1s} v_{is} \tag{38}$$

$$a(i,j,k,\ldots,n) = \sum_{s=1}^{M} c_s a_{ns} \omega_{is} \omega_{js} \ldots \omega_{ns} \tag{39}$$

$$b(i,j,k,\ldots,n) = \sum_{s=1}^{M} c_s a_{ns} v_{is} v_{js} \ldots v_{ns} \tag{40}$$

$$c(i,j,k,\ldots,n) = \frac{1}{2} \sum_{s=1}^{M} c_s a_{ns} \omega_{is} v_{js} \ldots \omega_{ns} v_{ns} \tag{41}$$

Hence, it has been shown that NARMA model coefficients are obtained from the proper training of a neural network. We employed a similar approach for the NAR model parameters estimation.

5.2 NAR model analysis

According to [20], the NAR model is given by the following formula:

$$y(n) = f(y(t-1), y(t-2), \ldots, y(t-d)) + e(t) \tag{42}$$

where f is the unknown smooth function, $y(t)$ is the output, t is the time vector, d is the number of delays, and $e(t)$ is the error term. We assume the error term $e(t)$ to be independent identically distributed (i.i.d.) and having the conditional mean $E(e(t)|f(t-1), f(t-2), \ldots)=0$ with the finite variance σ^2. The minimum mean square error optimal predictor of $y(t)$ given the past values $y(t-1)$, $y(t-2)$, $\ldots$, $y(t-d)$ is the conditional mean [20]:

$$\begin{aligned} \hat{y}(t) &= E(y(t)|y(t-1, y(t-2), \ldots, y(t-d)) \\ &= f(y(t-1), y(t-2), \ldots, y(t-d)) \end{aligned} \tag{43}$$

where $t \geq d+1$. The predictor has mean-squared error σ^2.

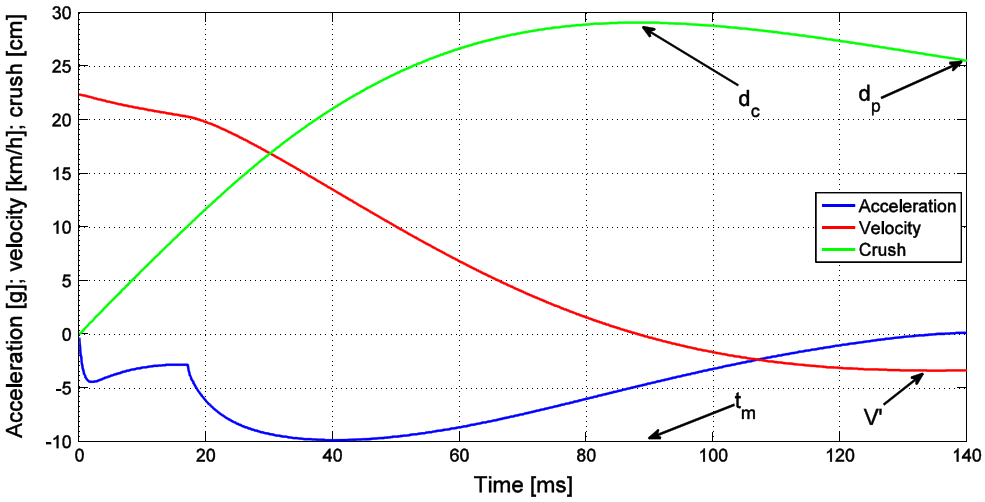

Fig. 26 Virtual car's kinematics

Table 7 Parameters characterizing the virtual collision

Parameter	Value
Initial impact velocity, V (km/h)	22
Rebound velocity, V' (km/h)	3.2
Maximum dynamic crush, d_c (cm)	29
Time when it occurs, t_m (ms)	88
Permanent deformation, d_p (cm)	25

5.3 Network's establishment

By following the same method as the one elaborated in [20], a feedforward neural network has been created as NAR model. It is a nonlinear approximation to function f given by:

$$\begin{aligned}\widehat{y}(t) &= \widehat{f}(y(t-1), y(t-2), \ldots, y(t-d)) \\ &= \sum_{i=1}^{I} W_i g\left(\sum_{j=1}^{d} w_{ij} y(t-j) + \theta_i\right)\end{aligned} \tag{44}$$

where the function $g(x)$ is a smooth bounded monotonic function—in our case, a sigmoid one. It is noted that the argument x of function $g(x)$ in (44) is referred to as a single neuron summation. Hence, the sigmoid activation function becomes:

$$g(x) = \frac{1}{1+e^{-x}} \tag{45}$$

I denotes the total number of neurons in the hidden layer. The parameters W_i and w_{ij} (weights) as well as θ_i (biases) are estimated in the training process—Levenberg–Marquardt backpropagation technique was used in this work. It was developed, e.g., to perform the network teaching without computing the Hessian matrix. It can be approximated as [59]:

$$H = J^T J \tag{46}$$

under the assumption that the network's performance function has the form of a sum of squares (feedforward network training procedure produces typically such an outcome). Moreover, the gradient can be expressed as:

$$g = J^T e \tag{47}$$

where J is the Jacobian matrix—it is composed of first derivatives of the network errors with respect to the weights and biases, and e is a vector which contains network errors. According to [60], computing Jacobian matrix using backpropagation technique is less complex than computing the Hessian matrix. The Levenberg–Marquardt backpropagation algorithm is given by (I stands for an identity matrix):

$$x_{k+1} = x_k - \left[J^T J + \mu I\right]^{-1} J^T e \tag{48}$$

Coefficient μ decides on the overall performance of the algorithm: when it is equal to zero, the approach degenerates into the Newton's method which uses the approximate Hessian matrix. On the other hand, when the value of μ increases, this becomes gradient descent. Newton's method works well near an error minimum, so it is advisable to shift to Newton's method right at the beginning of network training stage. Therefore, the decreasing performance function (i.e., improvement of network's accuracy) causes μ to decrease. μ increases, however, only when a tentative step would increase the performance function. Thanks to that, it is guaranteed that the performance function is always reduced at each iteration of the algorithm [61]. An estimation of the function f, i.e., $\widehat{f}$ from (44), is obtained by minimizing the sum of the squared residuals $\sum_{t=1}^{n} (y(t)-\widehat{y}(t))^2$, where n denotes the total number of time samples.

5.4 Network's structure and training

Multiple layer neural networks do not give any advantages for the time series problem as the one analyzed by us—it is not as complex as, e.g., speech recognition problem which requires consideration of a multilayer neural network [20]; therefore, it is sufficient to use just one hidden layer. Instead of using an optimization technique in the trial and error method, it was decided to select the number of input delays $d=5$ and the total number of neurons in the hidden layer $I=30$. The architecture of the network created by us is shown in Fig. 27. The validation of the results was done by using error histogram from Fig. 28, regression plot from Fig. 29, and training state from Fig. 30. As an input to the network, we have provided the real vehicle's recorded acceleration which consisted of 1,401 samples, being equal to the crash time period of 0.14 s sampled with the frequency of 10 kHz. In fact, this signal exhibits the most complex characteristic from all the other signals which we analyze. This guarantees the possibly best performance of a network when it is simulated to predict the signals which were not used for its creation. The time series data obtained from the experiments (real and virtual acceleration, respectively) was considered as a target data. The network is trained until the performance goal is met, i.e., until thesum of the squared residuals (or mean-squared error; MSE) $\sum_{t=1}^{n} (y(t)-\widehat{y}(t))^2$ reaches a value close to zero and does not improve after a few iterations (in our case, it is six validation checks). The good measure of the network's validation is illustrated in the so-called regression plot in Fig. 29 which determines whether the values estimated by an ANN are comparable with the target ones and in Fig. 30 which

represents the relationships between the number of iterations (epochs), validation checks, and gradient of the teaching curve. The measured real crash pulse used in the training of the network has been randomly divided into three parts in the following way:

- Training data: 50 %—the network is adjusted according to its error.
- Validation data: 25 %—it measures network generalization and stops the training when the generalization does not improve.
- Testing data: 25 %—it provides an independent measure of network performance during and after the training.

It means that the three above subsets have been chosen from target data provided to the network as the reference characteristic.

5.5 Network's performance

Training of the network stops when the generalization stops improving, as indicated by an increase in the mean square error of the validation samples. It turned out that after 53 iterations the performance (mean-squared error) did not improve; therefore, after six validation checks, the training was stopped. Plots of network's performance and error histogram are shown in Figs. 31 and 28, respectively. The output of the network is compared to the original signal used in the teaching stage in Fig. 32 (plots are named *Real reference* and *Real estimated*, respectively). Results obtained in this step are satisfactory. The value of the mean-squared error equals around to MSE=0.0065 and was achieved quickly—after 53 epochs. Considering the error distribution, almost 1000 of all the samples analyzed (being 71 % of the total number of samples) was reproduced with high degree of accuracy. The other 29 % of samples also exhibit great accuracy of prediction. Regression plots, showing correlation between the target values and the network's outputs are in Fig. 29. The value of regression $R=1$ means close relationship—no deviation from the original target values. We observe it for the each set of data: training, validation, and test. The training state is depicted in Fig. 30. There are illustrated parameters utilized in the Levenberg–Marquardt backpropagation algorithm. Exactly as supposed, μ starts to increase when the network's performance does not improve. Above considerations allow us to proceed to the evaluation of network's results in simulation of the data sets which were not used for its creation in the training stage.

5.6 Simulation results

Having the network trained and simulated for the dataset used for its creation (real car's acceleration), we proceed to evaluation of its capabilities of reproducing the kinematic plots, which were not used in the teaching stage. The outcome of this operation is presented in Figs. 32, 33, and 34. The simulation results illustrate that the network does not only reproduce the crash pulse signal which was utilized in the teaching procedure, but—what is of great significance—it predicts the kinematic responses which were not presented to it in its creation stage. This is because of the fact that the created mathematical model is a parametric one. It means that a given structure of a neural network can be used for testing of another signal as long as they have the same number of samples as the reference signal used in the training stage. Since for teaching, a signal which is the most complex among all the six pulses examined in this work has been used, the network is able to reproduce the other five less complex signals in the simulation and testing stages. Once the network is properly taught, it reproduces another signal without any fault. In the literature, there are not much examples of application of ANNs to reproduce kinematics of a vehicle undergoing a collision. On the other hand, NNs are commonly used in statistical models of vehicle crashes as already described. Therefore the contribution of this work is not only validation of the ANNs simulation results but also their application in an area which has not been extensively explored by their usage yet.

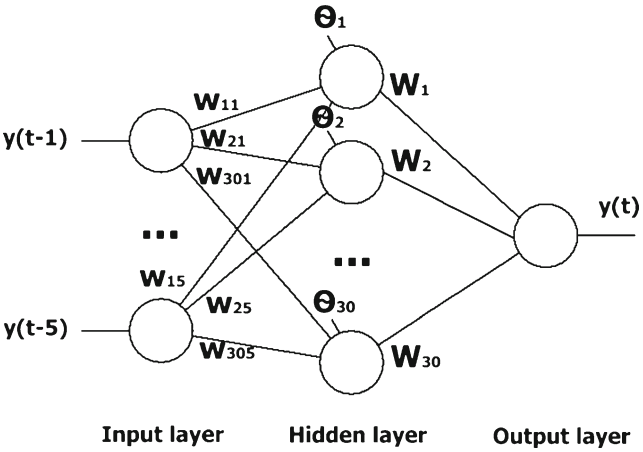

Fig. 27 Feedforward neural network's architecture

6 Signal reconstruction, modeling, and simulation based on Morlet wavelets

According to [33], one of the major contributions of this work is evaluation of the simulation results with the data obtained from a full-scale vehicle crash test. Furthermore, the wavelet-based modeling methodology is applied to vehicle crash modeling yielding reliable results. Finally, the fidelity of the created mathematical model is evaluated by comparing its results with the ones obtained by using different modeling approaches.

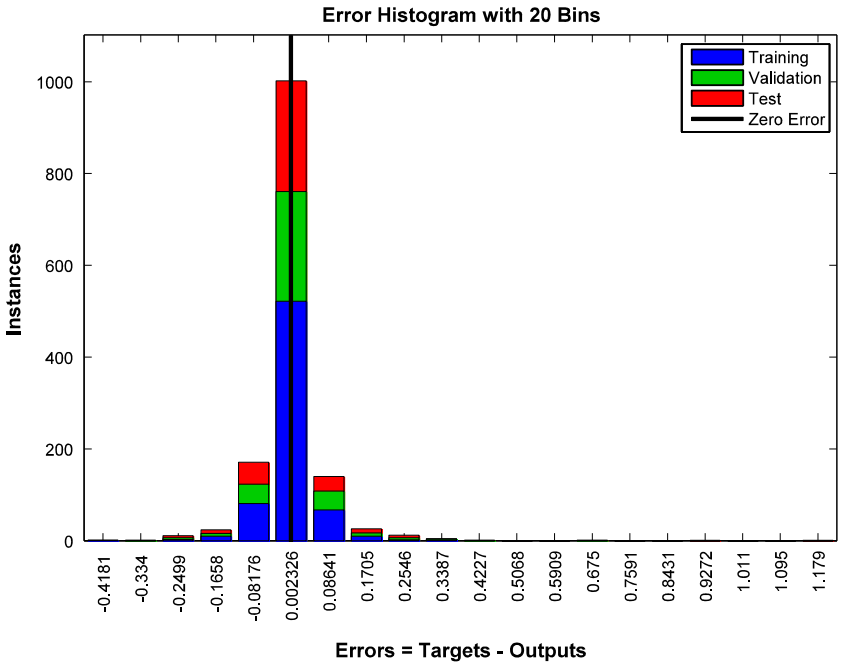

Fig. 28 Network's error histogram

6.1 Continuous wavelet transform (CWT)

Wavelet analysis is a method of signal decomposition [62]. Wavelet transform decomposes a signal into the elementary signals called wavelets. Wavelets are continuous, oscillatory functions which have diversified lasting times as well as spectra. The wavelet transform of a signal $x(t)$ which satisfies the condition:

$$\int_{-\infty}^{\infty} |x(t)|^2 dt < \infty \tag{49}$$

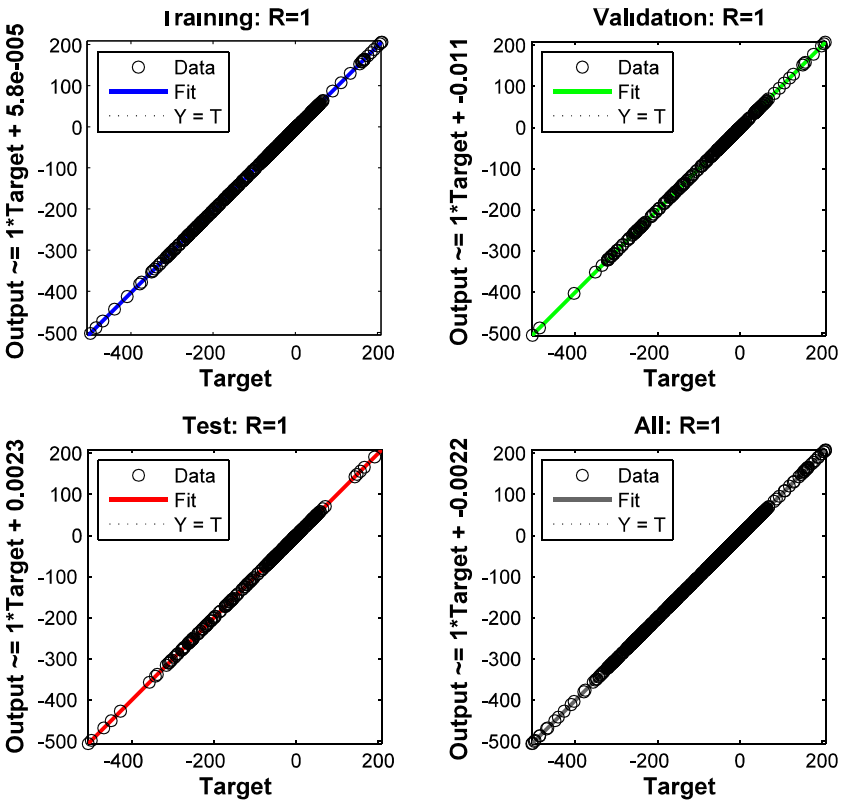

Fig. 29 Network's regression plot

Fig. 30 Network's training state

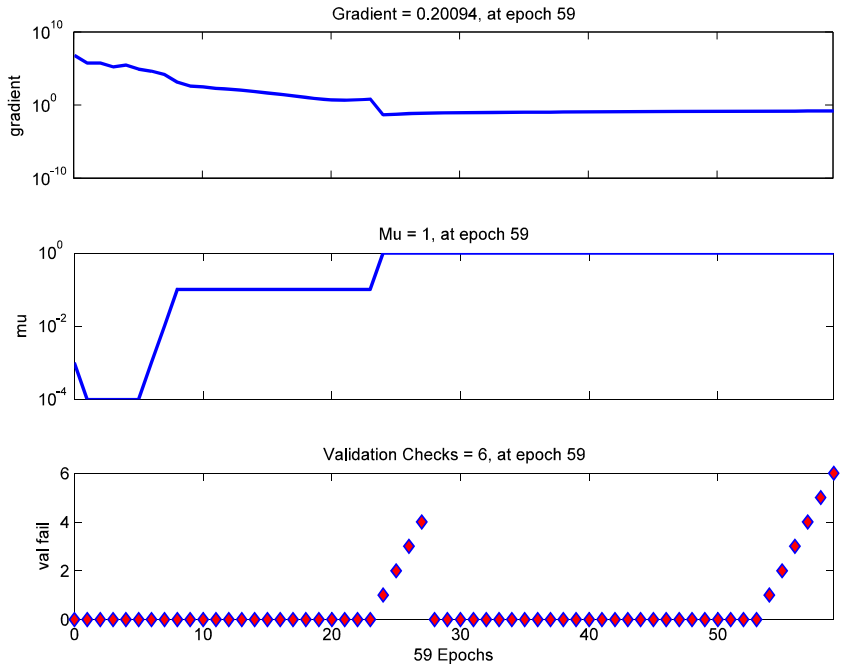

can be expressed as:

$$(W_g x)(a,b) = \frac{1}{\sqrt{a}} \cdot \int_{-\infty}^{\infty} x(t) g^* \left(\frac{t-b}{a} \right) dt \tag{50}$$

where:

b	translation value
a	scale parameter (dilation)
$g(t)$	elementary wavelet function
g^*	complex conjugate of function $g(t)$
$x(t)$	analyzed signal
t	time

Each value of $(W_g x)(a,\ b)$ is then normalized by the coefficient $\frac{1}{\sqrt{a}}$. This provides the condition that the internal energy of each wavelet $g_{a,b}(t)$ is independent of the scale parameter a. As it is seen from (50), wavelet transform can be considered as a linear transformation which decomposes a given signal $x(t)$ into elementary functions $g_{a,b}(t)$, which are

Fig. 31 Network's performance

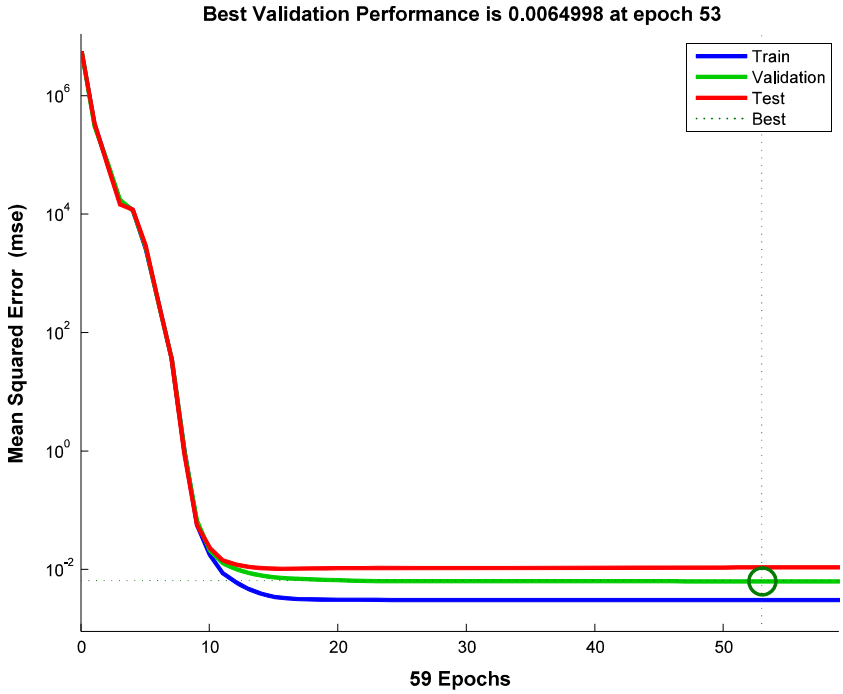

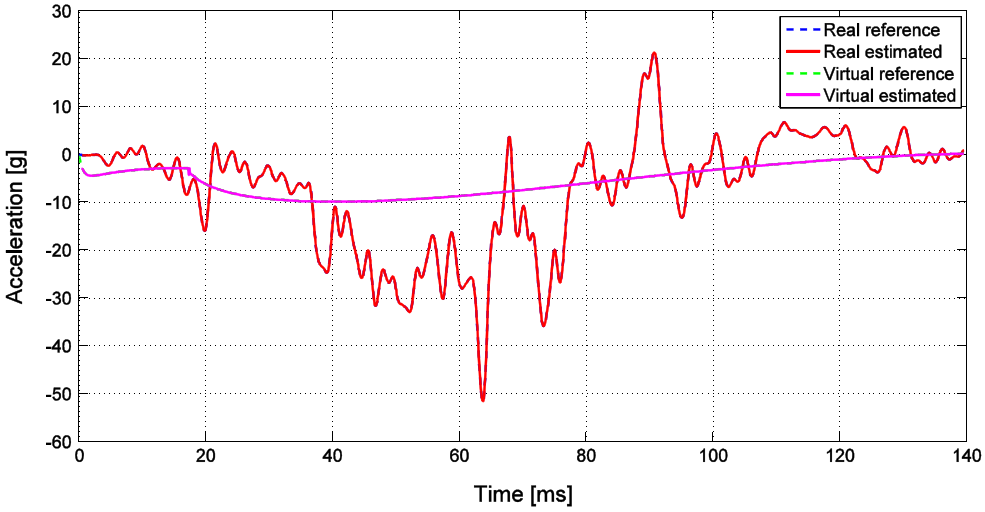

Fig. 32 Comparison of the measured and predicted acceleration for the real and virtual car

obtained from the wavelet function being analyzed $g(t)$ by dilation and translation. Translation b is related to time decomposition, whereas dilation a is responsible for frequency segmentation. This transformation has a significant advantage over the other transforms commonly used in engineering applications, e.g., Fourier transform, contrary to wavelet transform, does not provide local information about analyzed function because of the infinite character of the trigonometric functions which are utilized there.

6.2 Complex morlet wavelet

Morlet wavelet (named after Jean Morlet [63]) is defined as:

$$g(t) = e^{j2\pi f_0 |t|} \cdot e^{-\frac{|t|^2}{2}} \tag{51}$$

where:

j imaginary unit

f_0 wavelet function center frequency

t time

The exemplary Morlet wavelet is shown in Figs. 35 and 36.

Fourier spectrum of the Morlet wavelet is given by the translated Gauss function [62]:

$$G(f) = \sqrt{2}\pi e^{-2\pi^2 (f-f_0)^2}. \tag{52}$$

Wavelet transform is a linear representation of a signal [64]. Therefore, for n given functions x_i and n complex values α_i ($i=1, 2, \ldots, n$), the following equation holds:

$$W_g = \sum_{i=1}^{n} \alpha_i \cdot (W_g x_i)(a, b) \tag{53}$$

This essential property makes it possible to apply wavelet transform to analyze signals composed of numerous components which are characteristic for impulse response of a construction. Local resolution of wavelet transform in the time

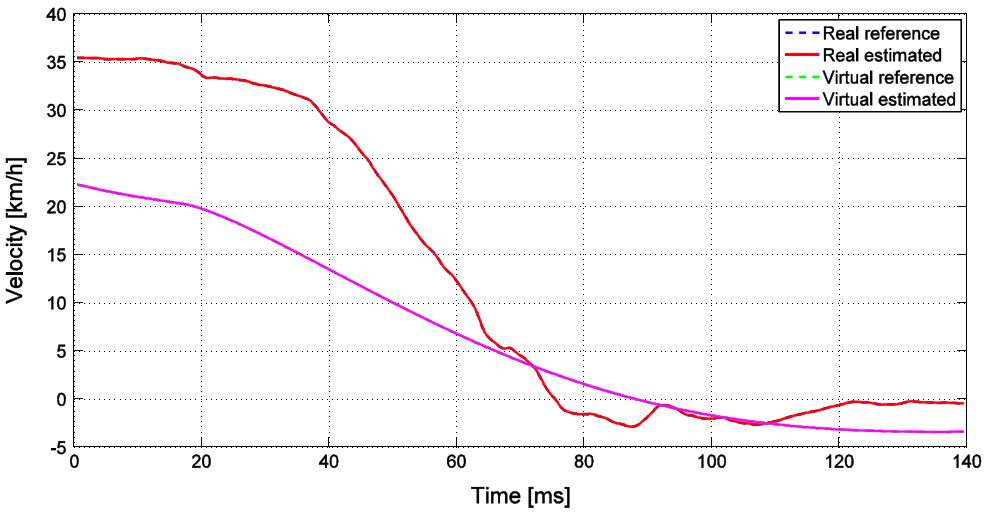

Fig. 33 Comparison of the measured and predicted velocity for the real and virtual car

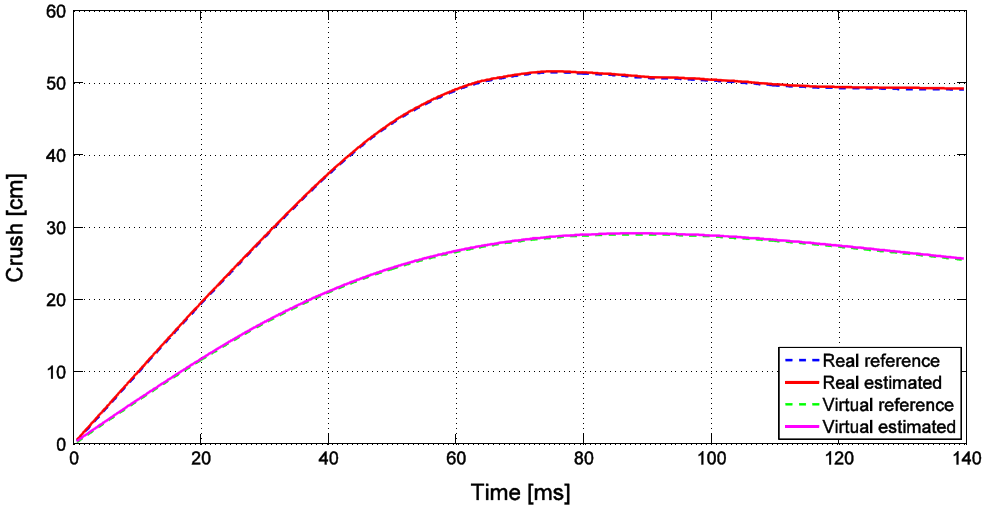

Fig. 34 Comparison of the measured and predicted crush for the real and virtual car

and frequency domains, respectively, is specified by the period and bandwidth of the frequency of an analyzed function:

$$\Delta t = a \cdot \Delta t_g \cdot \frac{1}{f_s} \tag{54}$$

$$\Delta f = \frac{\Delta f_g}{a} \cdot f_s \tag{55}$$

where Δt_g and Δf_g represent the period and bandwidth of the elementary wavelet function, respectively, and f_s is the sampling frequency of the analyzed signal. Equations (54) and (55) define relationships between scale parameter a, frequency resolution Δf, and time resolution Δt of the analyzed signal.

6.3 CWT parameters selection

It is an advantage of the continuous wavelet transform that it is possible to determine its coefficients for each value of the scale parameter a. Moreover, CWT is continuous with respect to the translation, which means that for a given scale value the elementary wavelet function is smoothly translated in the whole domain interval of the analyzed signal. The results obtained from such an approach are more convenient to interpret and emphasize some of the features contained in the signal as well. The drawback of CWT is, however, its great computational complexity.

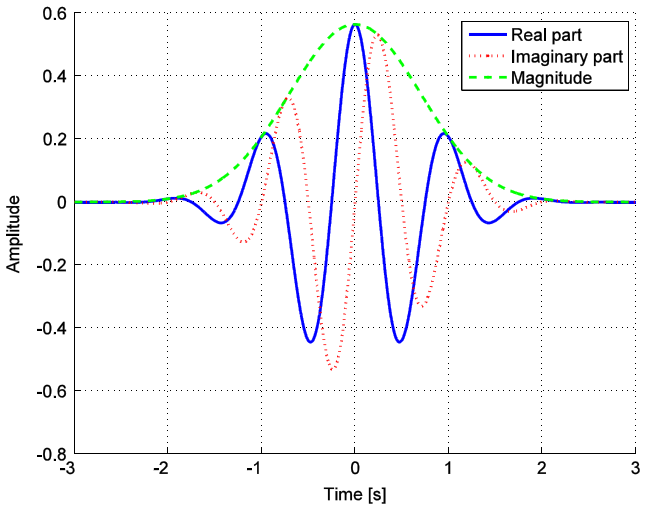

Fig. 35 Exemplary complex Morlet wavelet components

The key issue related to wavelet analysis is the proper choice of its parameters [62]. The elementary wavelet function $g(t)$ concentrates the majority of its energy in the interval $(\omega_{\min}, \omega_{\max})$. The Fourier transform $G(\omega)$ outside of this interval is omitted, hence spectrum g_{mn} of $g(t)$ has significant values in the interval $(\omega_{\min}/2^m, \omega_{\max}/2^m)$. For low values of the scale parameter a, high-frequency components of the signal are extracted, whereas the low-frequency components require high values of the scale parameter a as it is shown by (55). Therefore, if we select a narrow bandwidth of the elementary wavelet function $g(t)$, we emphasize those features of the signal which last for a short period of time; however, we lose the resolution in the time domain. Contrary, if we choose a wide bandwidth, the time features of the signal are reproduced well but simultaneously we lose the resolution in the frequency domain.

6.4 Scale gram creation

According to [65], a scale gram is a measure of the variances of the wavelet coefficients (i.e., strength of the signal) as a function of the time scale. Formulation of the wavelet coefficients matrix is achieved by translating and scaling elementary wavelet functions and subsequently translating them along the time axis of the analyzed signal. The convolution of wavelet function and analyzed signal which is obtained in this step gives the values of the wavelet coefficients matrix. Schematically, this process is visualized in Fig. 37. It is noted that the execution of the block diagram from Fig. 37 was performed in

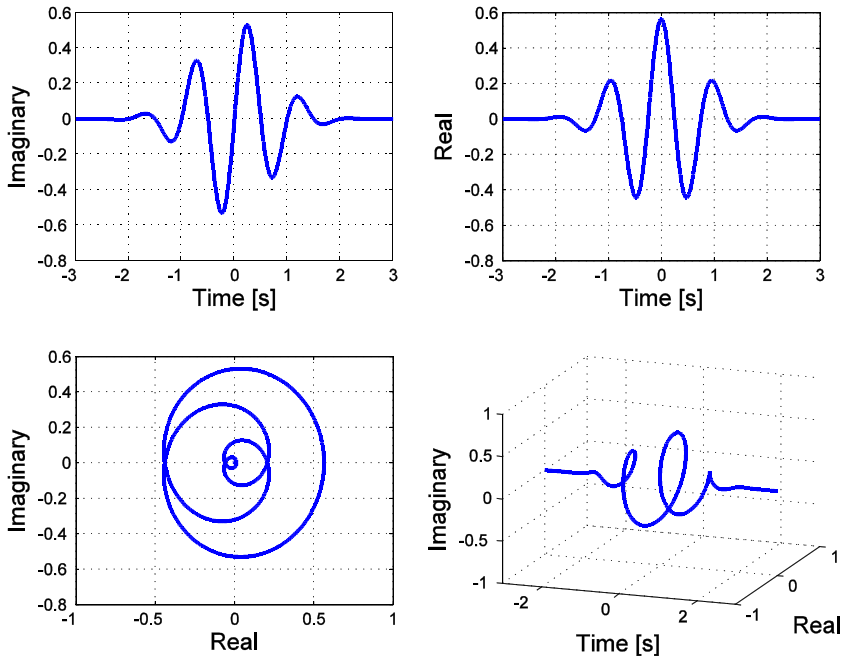

Fig. 36 Complex Morlet wavelet components—overview

MATLAB® software—for the details regarding the step-by-step procedure, refer to [66]. The characteristic feature of a scale gram is its changeable resolution in the time and frequency domains. In this work, we will also use the notions of ridge and skeleton of the wavelet transform, which are described according to [62].

1. Ridge of the wavelet transform—is a set of points (a, b) in the domain of the wavelet transform $(W_g x)(a, b)$ of the signal $x(t)$ where the phase $x(t)g_{(a,b)}(t)$ is stationary, so the following condition is satisfied:

$$t_0(a, b) = b \tag{56}$$

The simplest method to detect a ridge of the wavelet transform is to find the maximum values of the wavelet coefficients in the wavelet coefficients matrix.

2. Skeleton of the wavelet transform—is a set of coefficients of the wavelet transform $(W_g x)(a, b)$ calculated from the ridge $(W_g x)(a_r(b), b)$ where a_r is the scale parameter of the ridge.

6.5 Signal reconstruction

The above two definitions have a strong impact on the interpretation of the wavelet analysis results, since in practical applications, the skeleton of the wavelet transform is required to reconstruct a signal for a given frequency component. On the other hand, the knowledge of the ridge of the wavelet transform leads to determination of the frequency components of a signal. Therefore, the natural frequency of a system can be obtained directly from the ridge, whereas the skeleton contains information about response of a system in time domain.

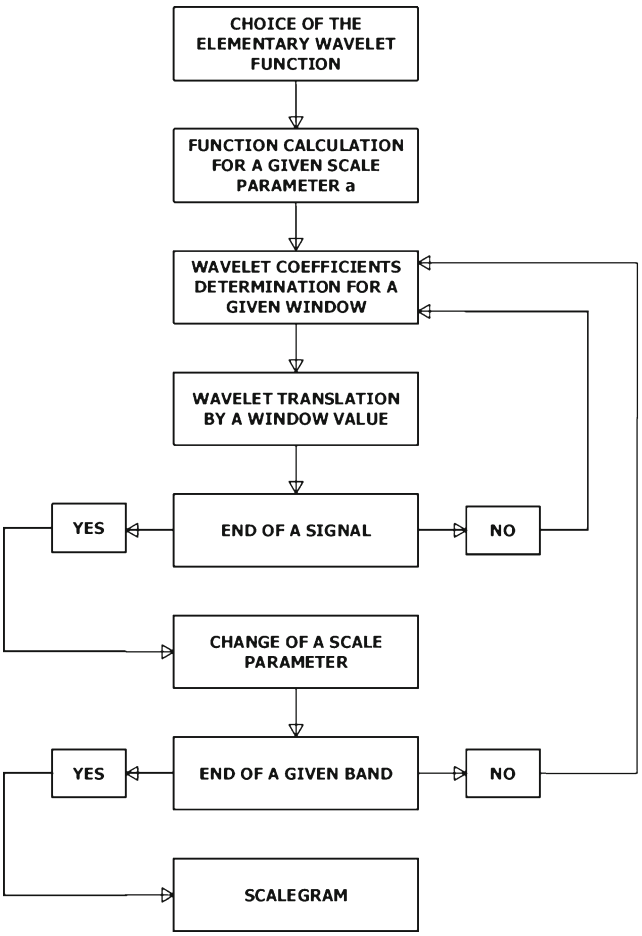

Fig. 37 Block diagram for scale gram creation

Since by using CWT, a one-dimensional signal is mapped to a two-dimensional signal, it causes a lot of redundancy in the representation of the signal. However, it provides the possibility for signal reconstruction. A classical inversion formula is [67]:

$$x(t) = C_g^{-1} \iint W(a,b) g_{a,b}(t) \frac{da}{a^2} db. \tag{57}$$

There exists, however, a simpler inverse way which requires using Morlet's formula. In this method, only single integration is needed:

$$x(t) = C_{1g}^{-1} \int W(a,b) \frac{da}{a^{3/2}} \tag{58}$$

where:

$$C_{1g} = \int_{-\infty}^{\infty} \frac{g^*(\omega)}{|\omega|} d\omega \tag{59}$$

Therefore, (58) is used to reconstruct a signal for the scale parameters for which coefficients of the wavelet transform matrix have the maximum values—i.e., for the scale parameters for which ridges are detected.

6.6 Data analysis

We apply the presented methods to the acceleration pulse recorded in x-direction during the collision of a vehicle with a barrier (Fig. 38). We choose complex Morlet wavelet as an elementary wavelet function: bandwidth and center frequencies are selected to be f_b=2 Hz and f_0=2 Hz, respectively. Their values are assigned in the trial-and-error process according to the dataset being analyzed (i.e., its length and sampling rate). The general rule here is that the center frequency based approximation should capture the main wavelet oscillation. In other words, the leading dominant frequency of the wavelet is characterized by the center frequency of the elementary wavelet function [66]. Consequently, when we relate the frequency f_0 with the wavelet function and dilate the wavelet by a factor a, the center frequency becomes f_0/a. Finally, by taking into account the sampling frequency f_s and applying Eq. 55 (as it is shown below), the frequency vector is derived. Based on Eq. 51, the following elementary wavelet function is obtained: Fig. 39.

Based on the frequency components information obtained from Fourier transform of the analyzed acceleration signal (see Fig. 40), the frequency range in which all the relevant frequency components of the analyzed signal are contained are defined. This frequency interval according to (55) determines the size of the scale vector for wavelet coefficients matrix:

$$a_{\min} = \frac{\Delta f_g}{f_{\max}} \cdot f_s \tag{60}$$

$$a_{\min} = \frac{2[\mathrm{Hz}]}{625[\mathrm{Hx}]} \cdot 10,000 = 32 \tag{61}$$

$$a_{\max} = \frac{\Delta f_g}{f_{\min}} \cdot f_s \tag{62}$$

$$a_{\max} = \frac{2[\mathrm{Hz}]}{28.5714[\mathrm{Hz}]} \cdot 10,000 = 700 \tag{63}$$

According to (50), the wavelet transform is performed and matrix of wavelet coefficients is calculated. The scale gram showing wavelet coefficients matrix obtained in this operation is illustrated in Fig. 41. Please note the scale gram from Fig. 41 is plotted in the scale–samples relationship. By using relationship given by (55), it is possible to plot the scale gram in the frequency time domain (see Figs. 42 and 43). This gives the better understanding of the CWT, since the relationship between the frequency components of the acceleration pulse and the time intervals when they are present is explicitly presented. Please note that on Fig. 43, there are also plotted ridges of the wavelet coefficients matrix for five frequency components which are considered to have the greatest influence on the scale gram of the acceleration signal, i.e., which have the highest amplitudes. The ridges are detected by using the discussed method, i.e., they are the local maxima of the coefficients of the wavelet coefficients matrix. Table 8 summarizes the values of identified frequency components of the acceleration signal and the scale parameters for which the highest values of coefficients of wavelet coefficients matrix (i.e., ridges) are observed.

Remark 1. *It is noting that the computational aspect of the wavelet coefficients matrix creation has a crucial influence on the simulation results. In the case being considered, the obtained wavelet coefficients matrix was of size 669× 1,751. This is due to the length of the signal being analyzed and to the size of the assumed frequency vector. Simulations were performed on a 4 GB RAM PC with four-core, eight-thread processor each of 1.6 GHz clock speed being able to boost up to 2.8 GHz in a max turbo frequency mode. The computational time needed to create the wavelet coefficients matrix of the size mentioned above was 12.022 s. In some cases of much larger wavelet coefficients matrices, one needs to consider the maximum memory capacity of a computer used so that the simulation becomes possible whatsoever.*

The acceleration signal contains a huge number of frequencies, as shown in Fig. 40. Therefore, it is considered as a sum signals which have this wide range of frequencies. For this reason, the superposition principle holds here—reconstruction of the acceleration signal is achieved by adding its signal components, which have the major frequencies (of the highest

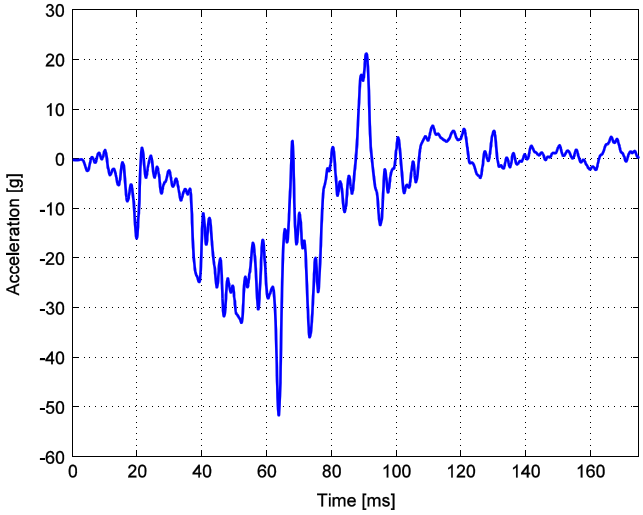

Fig. 38 Vehicle acceleration pulse recorded during a collision

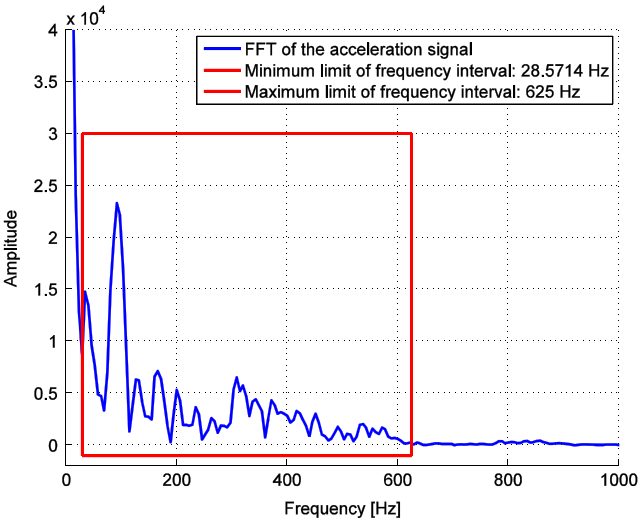

Fig. 40 Fast Fourier transform of the acceleration signal in x-direction

CWT amplitude). CWT helps to identify not only the frequencies of those component signals, but also their time history (see Fig. 20).

6.7 Simulation results

To reconstruct the acceleration signal shown in Fig. 38, (58) is used. We sum the real part of wavelet coefficients matrix components for the scale parameters for which the highest amplitudes of CWT were observed—i.e., for the frequency components for which ridges are determined. Literally, it may be described as adding the skeletons of the wavelet transform. Since five main frequency components of the acceleration signal have been identified, reconstruction of this signal is achieved by summation of the skeletons of those five ridges, which are shown in Fig. 44. The resulting reconstructed acceleration signal is presented in Fig. 45. To obtain velocity and displacement of the vehicle throughout the collision, it is required to integrate the estimated acceleration signal. Results of this operation are illustrated in Figs. 46 and 47. It is shown that the overall behavior of the estimated acceleration curve follows the reference acceleration. Consequently, the similarities between estimated and reference velocities as well as displacements are observed.

7 Conclusions and future works

The obtained results indicate that the spring–mass and Kelvin models are not appropriate for simulation of the collision which we deal with. However, results obtained from studying Maxwell model provided us with more satisfactory results.

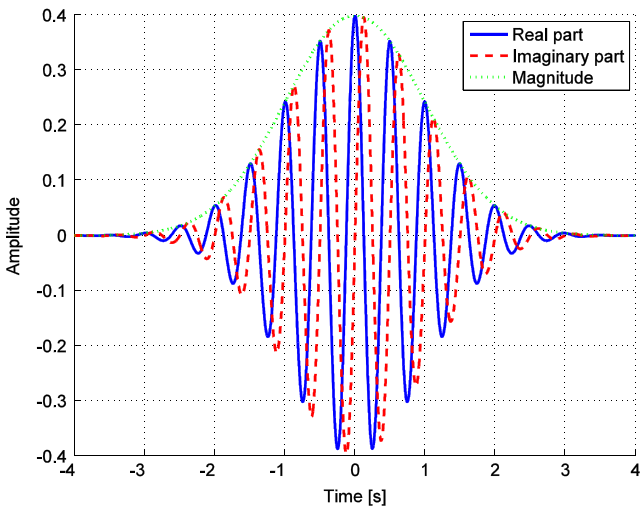

Fig. 39 Elementary wavelet function—complex Morlet wavelet

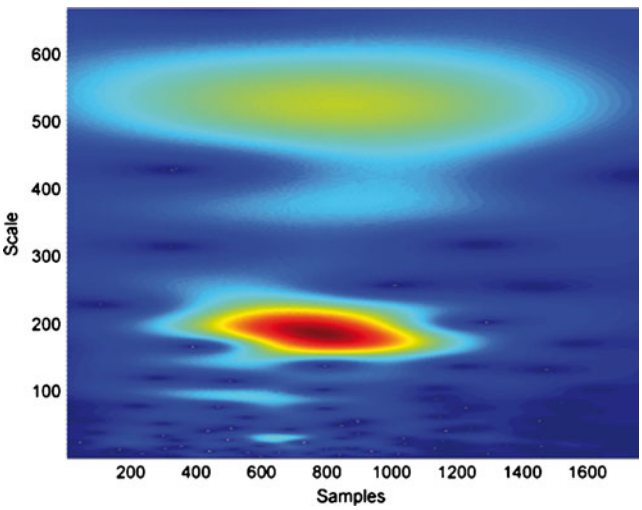

Fig. 41 Scale gram of the acceleration signal

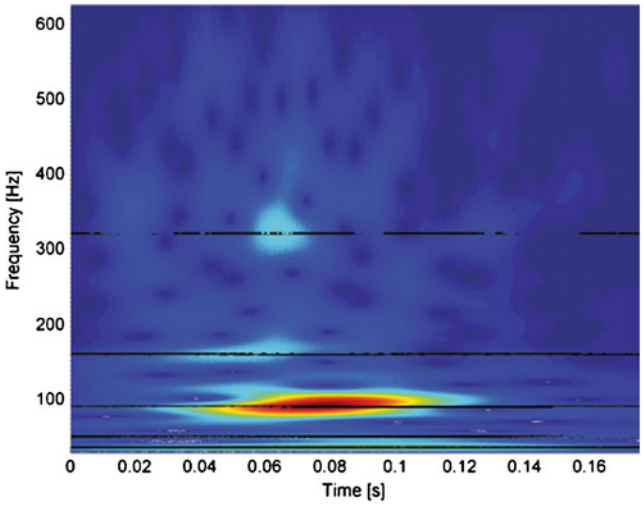

Fig. 42 Scale gram of the acceleration signal seen from top: frequency time domain. Ridges of the wavelet coefficient matrix are also shown

Comparative analysis of the model's and real car's responses allows to conclude that the obtained simulation outcomes closely resemble the original full-scale vehicle behavior.

It is desirable to verify whether the other viscoelastic models which were not discussed in this paper are capable of vehicle crash simulation. In particular, the so-called hybrid models (systems composed of two springs, one damper, and a mass) may be promising for this application. Furthermore, a two-mass–spring–damper model can be used to represent interactions between fore- and aft-frame of a vehicle. On top of that, it is advisable to examine methods for nonlinear system parameters identification. Since the models presented in Section 3 are lumped parameter ones, which are valid only for the data which were used for their creation, they cannot be used to simulate, e.g., a high-speed vehicle collision. However, the capabilities of mathematical models with nonlinear parameters (stiffness and damping) to simulate a variety of crash events are required to be assessed.

Table 8 Main frequency components of the acceleration signal

Scale	Frequency (Hz)
62.5	320
125	160
222	90
400	50
555	36

One of the preponderant advantages of the wavelet transform is its applicability to analysis of signals which represent nonstationary or nonlinear processes. For those systems, the classical approach in which we assume the constancy of parameters in linear systems is not sufficient. As already mentioned, Fourier transform does not allow for detection of local features of signals, since the carriers of this operation are trigonometric functions, which by definition have nonbounded character. By analyzing a signal in the frequency domain, we gain insight into its spectrum; however, we know nothing about the time when particular peaks occur. On the other hand, when we know their localization in time, we know nothing about their frequency. In order to avoid this difficulty, it is advisable to use wavelet transform. In this type of analysis, we limit the frequency bandwidth (i.e., the resolution of analysis) only to the frequencies which are relevant for a given phenomenon. Therefore, one may say that by per forming a

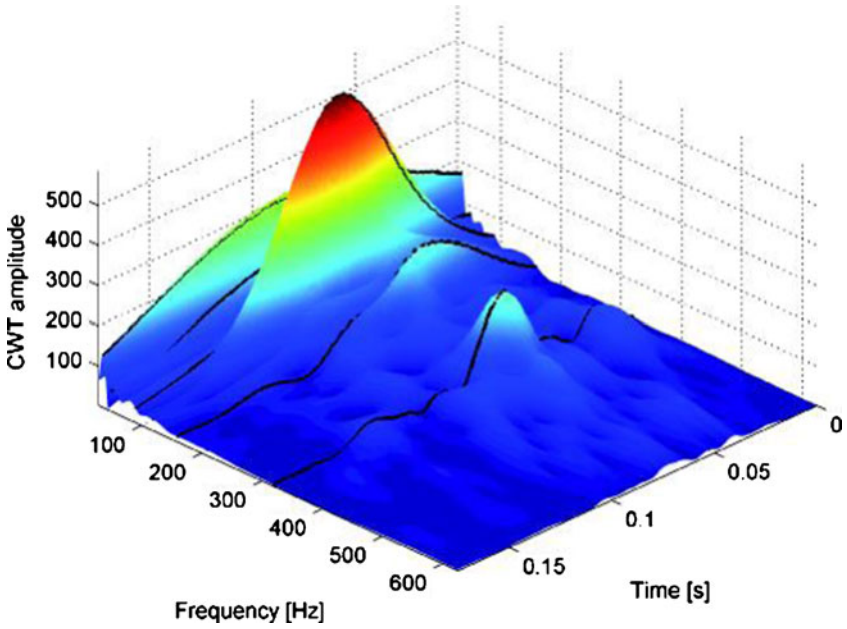

Fig. 43 Scale gram of the acceleration signal seen from side: frequency time domain. Ridges of the wavelet coefficient matrix are also shown

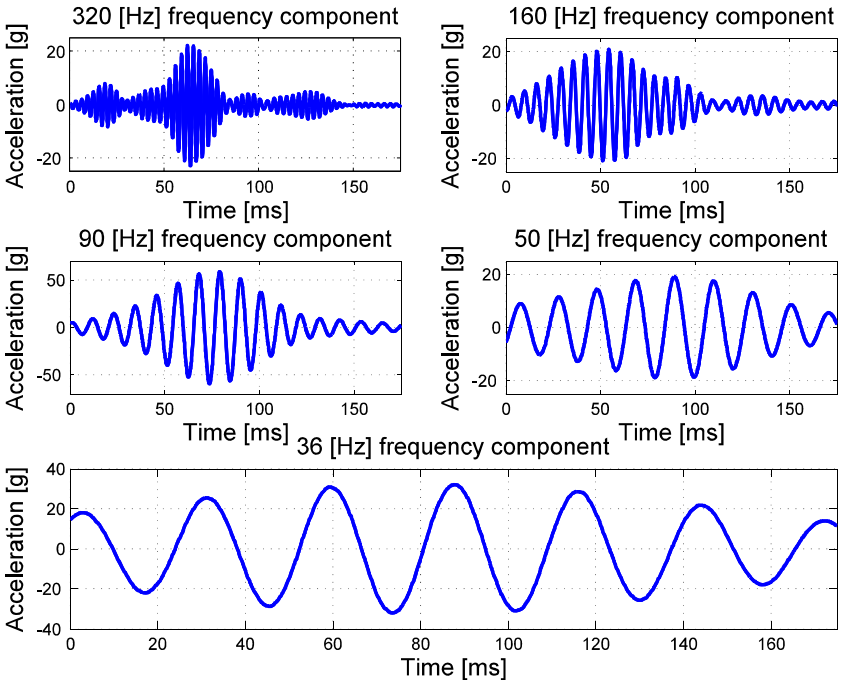

Fig. 44 Skeletons of the wavelet transform for the major frequency components of the acceleration pulse

wavelet transform, we approximate a physical phenomenon. The aim of this approximation is to extract the characteristic features of a process being considered from the signals which represent it.

Wavelet transform has a strong potential in modeling of real world physical systems. However, there are prerequisites that need to be addressed to properly perform system identification. One of those is the selection of proper frequency interval in which wavelet analysis is to be performed, according to the frequency components of signals which characterize a given phenomenon. It is noting that by executing wavelet transform, a given phenomenon is approximated. That is because if a narrow frequency band of an elementary wavelet function is assumed, local features of a signal are emphasized at the cost of resolution loss in the time domain. On the other hand, if a wide frequency band is assumed, time history features of a signal are reproduced well at the cost of resolution loss in frequency domain. It was showed in this work that to reproduce a given signal, it is sufficient to use only the major frequency components which have the highest amplitude among all the frequencies contained in the signal, i.e., frequency components for which ridges of the wavelet coefficients matrix are detected. It is emphasized that ridges for constant-scale parameters were assumed for the sake of

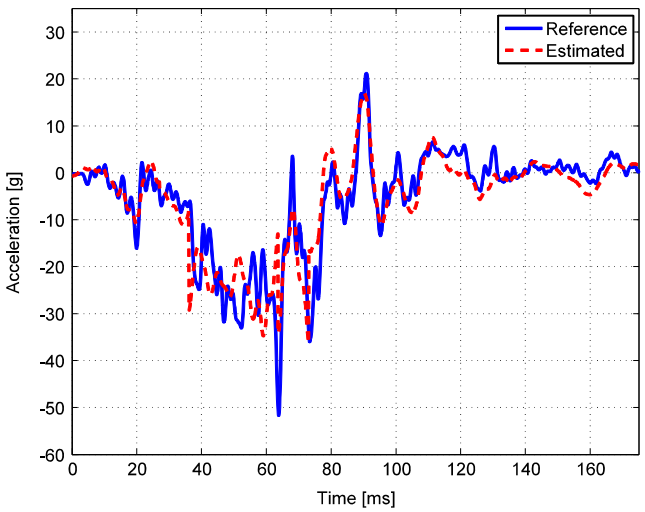

Fig. 45 Comparative analysis of the vehicle acceleration signals

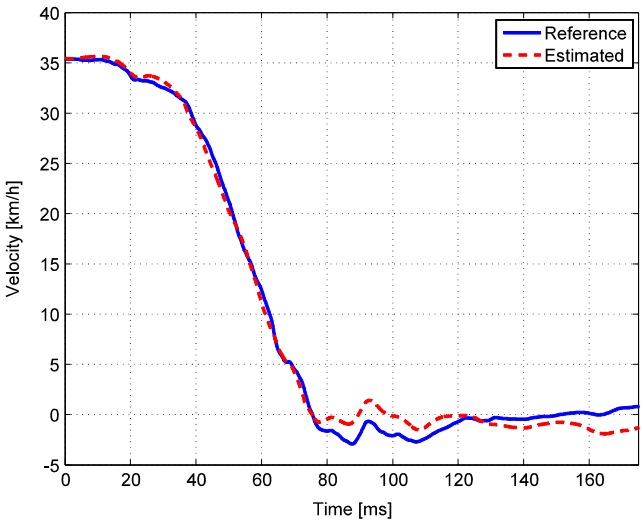

Fig. 46 Comparative analysis of the vehicle velocities

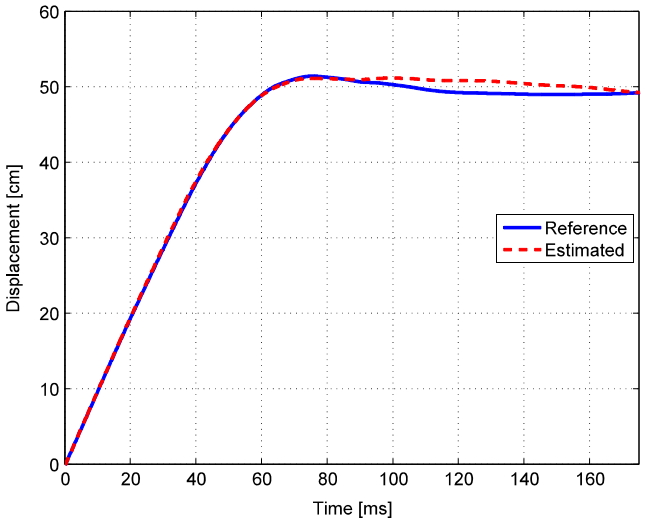

Fig. 47 Comparative analysis of the vehicle displacements

computational efficiency, however, still yielding reliable results. For the future work, it is recommended to introduce ridges for nonstationary signals, i.e., for changeable scale parameters. This will give a more accurate insight into the frequency domain part of analysis of a given signal and allow to detect its nonstationary frequency components.

NAR model was established and its capabilities of reproducing kinematics of a car in a crash event were evaluated. It was verified that for the NAR model, increasing the number of delays in a network will improve the model construction and the results of its testing as well. A similar case occurs for the number of neurons. The more neurons compose a hidden layer, the better is the network's prediction of a given signal. However, it was found that at some point (i.e., at some value of a delay, which is different for different signals we use), the increase of neurons number does not improve the results—in some cases, the data is even overfitted. Moreover, too huge amount of neurons greatly raises the computation time needed to teach a network. Therefore, a good network performance is a resultant of the proper selection of delays and number of neurons. On top of that, the appropriate division of the data set being examined, into teaching, validation, and testing sets can significantly enhance the overall network design (i.e., there is required less number of delays, neurons, and shorter computation time is needed to achieve the desired performance).

Neural networks have strong potential in nonlinear systems modeling—they can estimate their nonlinear parameters (e.g., stiffness and damping). The changeable initial impact velocity can be treated as an input to such a model and its output kinematics will help to predict a real car behavior. For instance, the application of the regressive models established for a low-speed collision to reproduce kinematics of a car involved in a high-speed collision may be investigated as well.

In order to visualize the effectiveness of each of the methods presented in this work, it was decided to calculate for every proposed modeling methodology the root mean square error (RMSE) of the estimated vehicle acceleration (y_i, reference value; $\widehat{y_i}$, estimated value):

$$\mathrm{RMSE} = \sqrt{\frac{\sum_{i=1}^{n}\left(y_i - \widehat{y_i}\right)^2}{n}} \tag{64}$$

which yields the results shown in Table 9. The value of the root mean square error determines the average difference between the reference and estimated value.

Table 9 clearly points out the significant improvement in the results of modeling vehicle crash by using wavelet-based method described in this work with respect to the results yielded by typical lumped-parameter models. However, the biggest benefit is obtained when approach based on nonlinear autoregressive model and feedforward neural network is followed.

Table 9 Values of root mean square error (RMSE)

Modeling methodology	RMSE for acceleration (g)
LPM–Kelvin model	10.49
LPM–Maxwell model	8.60
Wavelet-based method	5.22
NAR model and FFNN	0.08

References

1. Eskandarian A, Marzougui D, Bedewi NE (1997) Finite element model and validation of a surrogate crash test vehicle for impacts with roadside objects. Technical report, National Crash Analysis Center, Virginia, USA
2. Tenga TL, Chang FA, Liu YS, Peng CP (2008) Analysis of dynamic response of vehicle occupant in frontal crash using multibody dynamics method. Math Comput Model 48(11–12):1724–1736
3. Kim HS, Kang SY, Lee IH, Park SH, Han DC (1996) Vehicle frontal crashworthiness analysis by simplified structure modeling using nonlinear spring and beam elements. Int J Crashworthiness 2(1):107–118
4. Niu Y, Shen W, Stuhmiller JH (2007) Finite element models of rib as an inhomogeneous beam structure under high-speed 11 impacts. Med Eng Phys 29(7):788–798
5. Moumni Z, Axisa F (2004) Simplified modelling of vehicle frontal crashworthiness using a modal approach. Int J Crashworthiness 9(3): 285–297
6. Borovinsek M, Vesenjak M, Ulbin M, Ren Z (2007) Simulation of crash tests for high containment levels of road safety barriers. Eng Fail Anal 14(8):1711–1718
7. Soto CA (2004) Structural topology optimization for crashworthiness. Int J Crashworthiness 9(3):277–284

8. Belytschko T (1992) On computational methods for crashworthiness. Comput Struct 42(2):271–279
9. Deb A, Srinivas KC (2008) Development of a new lumped parameter model for vehicle side-impact safety simulation. In: Proceedings of the Institution of Mechanical Engineers, Part D: Journal of Automobile Engineering, vol. 222, pp.1793–1811
10. Jonsén P, Isaksson E, Sundin KG, Oldenburg M (2009) Identification of lumped parameter automotive crash models for bumper system development. Int J Crashworthiness 14(6):533–541
11. Šušteršić G, Grabec I, Prebil I (2007) Statistical model of a vehicle-to-barrier collision. Int J Impact Eng 34(10):1585–1593
12. Elmarakbi AM, Zu JW (2006) Crash analysis and modeling of two vehicles in frontal collisions using two types of smart front-end structures: an analytical approach using IHBM. Int J Crashworthiness 11(5):467–483
13. Pawlus W, Karimi HR, Robbersmyr KG (2011) Mathematical modeling of a vehicle crash test based on elasto-plastic unloading scenarios of spring–mass models. Int J Adv Manuf Technol 55:369–378
14. Pawlus W, Karimi HR, Robbersmyr KG (2011) Development of lumped-parameter mathematical models for a vehicle localized impact. J Mech Sci Technol 25(7):1737–1747
15. Pawlus W, Karimi HR, Robbersmyr KG (2011) Effects of different spring–mass model elasto-plastic unloading scenarios on the vehicle crash model fidelity. ICIC Expr Lett Part B Appl 2(4):757–764
16. Pawlus W, Karimi HR, Robbersmyr KG (2011) Application of viscoelastic hybrid models to vehicle crash simulation. Int J Crashworthiness 16(2):195–205
17. Pawlus W, Robbersmyr KG, Karimi HR (2011) Mathematical modeling and parameters estimation of a car crash using data-based regressive model approach. Appl Math Model 35:5091–5107
18. Ma J, Kockelman KM, Damien P (2008) A multvariate Poisson-lognormal regression model for prediction of crash counts by severity, using Bayesian methods. Accid Anal Prev 40(3):964–975
19. Pawlus W, Karimi HR, Robbersmyr KG (2012) Data-based modeling of vehicle collisions by nonlinear autoregressive model and feedforward neural network. Inf Sci. doi:10.1016/j.ins.2012.03.013, ISSN: 0020-0255
20. Connor JT, Martin RD, Atlas LE (1994) Recurrent neural networks and robust time series prediction. IEEE Trans Neural Netw 5(2):240–254
21. Crucianu M, Uhry Z, Boné R, Asselin de Beauville J-P NAR time-series prediction: a Bayesian framework and an experiment. Proceedings of the European Symposium on Artificial Neural Networks (ESANN '98), Bruges, Belgium, April 1998
22. Wang D, Lum K-Y, Yang G (2002) Parameter estimation of ARX/NARX model: a neural network based method. Proceedings of the 9th International Conference on Neural Information Processing (ICONIPOZ), Singapore
23. Yang G, Lin Y, Bhattacharya P (2010) A driver fatigue recognition model based on information fusion and dynamic Bayesian network. Inf Sci 180(10):1942–1954
24. Pham HT, Tran VT, Yang B-S (2010) A hybrid of nonlinear autoregressive model with exogenous input and autoregressive moving average model for long-term machine state forecasting. Expert Syst Appl 37(4):3310–3317
25. Zvejnieks G, Kuzovkov VN, Dumbrajs O, Degeling AW, Suttrop W, Urano H, Zohm H (2004) Autoregressive moving average model for analyzing edge localized mode time series on Axially Symmetric Divertor Experiment (ASDEX) Upgrade tokamak. Phys Plasmas 11(12):5658–5667
26. Basso M, Giarré L, Groppi S, Zappa G (2005) NARX models of an industrial power plant gas turbine. IEEE Trans Control Syst Technol 13(4):599–604
27. Zemouri R, Gouriveau R, Zerhouni N (2010) Defining and applying prediction performance metrics on a recurrent NARX time series model. Neurocomputing 73(13–15):2506–2521
28. Crone SF, Kourentzes N (2010) Feature selection for time series prediction—a combined filter and wrapper approach for neural networks. Neurocomputing 73(10–12):1923–1936
29. Sheta AF, Jong KD (2001) Time-series forecasting using GA-tuned radial basis functions. Inf Sci 133(3–4):221–228
30. Gandhi UN, Hu SJ (1995) Data-based approach in modeling automobile crash. Int J Impact Eng 16(1):95–118
31. Bock J, Hettenhausen J (2012) Discrete particle swarm optimisation for ontology alignment. Inf Sci 192:152–173
32. Karimi HR, Robbersmyr KG (2011) Signal analysis and performance evaluation of a vehicle crash test with a fixed safety barrier based on Haar wavelets. Int J Wavelets Multiresolution Image Process 9(1):131–149
33. Karimi HR, Pawlus W, Robbersmyr KG (2012) Signal reconstruction, modeling and simulation of a vehicle full-scale crash test based on Morlet wavelets. Neurocomputing 93:88–99, ISSN: 0925-2312
34. Gan M, Peng H, Peng X, Chen X, Garba I (2010) A locally linear RBF network-based state-dependent AR model for nonlinear time series modeling. Inf Sci 180(no.22):4370–4383
35. Mitrakis NE, Theocharis JB (2012) A diversity-driven structure learning algorithm for building hierarchical neuro-fuzzy classifiers. Inf Sci 186(1):40–58
36. McFadden J, Yang WT, Durrans RS (2001) Application of artificial neural networks to predict speeds on two-lane rural highways. Transp Res Rec 1751:9–17
37. Abedelwahab H, Abdel-Aty MA (2001) Development of artificial neural networks models to predict driver injury severity in traffic accidents at signalized intersections. Transportation Research Board 80th annual meeting, Washington D.C., USA
38. Várkonyi-Kóczy AR, Rövid A, Várlaki P Intelligent methods for car deformation modeling and crash speed estimation. The 1st Romanan–Hungarian Joint Symposium on Applied Computational Intelligence, Timisoara, Romania, May 2004
39. Syrris V, Petridis V (2011) A lattice-based neuro-computing methodology for real-time human action recognition. Inf Sci 181(10): 1874–1887
40. van der Laan E, Veldpaus F, de Jager B, Steinbuch M LPV modeling of vehicle occupants. 9th International Symposium on Advanced Vehicle Control (AVEC '08), Kobe, Japan, October 2008
41. Zhang L, Shi P (2008) L_2–L_∞ model reduction for switched LPV systems with average dwell time. IEEE Trans Autom Control 53(10): 2443–2448
42. Zhang L, Cui N, Liu M, Zhao Y (2011) Asynchronous filtering of discrete-time switched linear systems with average dwell time. IEEE Trans Circ Syst I Regular Pap 58(5):1109–1118
43. Zhao Y, Zhang L, Shen S, Gao H (2010) Robust stability criterion for discrete-time uncertain Markovian jumping neural networks with defective statistics of modes transition. IEEE Trans Neural Netw 22(1):164–170
44. Cheng Z, Pilkey WD, Darvish K, Hollowell WT, Crandall JR (2001) Correlation analysis of automobile crash responses using wavelets. Proceedings of the International Modal Analysis Conference IMAC, Kissimmee, Florida, USA
45. Cheng Z, Pellettiere JA, Rizer AL (2004) Wavelet-based validation methods and criteria for finite element automobile crashworthiness modeling. Proceedings of the 22nd IMAC Conference and Exposition (IMAC XXII): A Conference and Exposition on Structural Dynamics, Dearborn, MI, USA
46. Kankar PK, Sharma SC, Harsha SP (2011) Rolling element bearing fault diagnosis using wavelet transform. Neurocomputing 74(10): 1638–1645
47. Hester D, Gonzalez A (2012) A wavelet-based damage detection algorithm based on bridge acceleration response to a vehicle. Mech Syst Signal Process 28:145–166
48. Nguyen KV, Tran HT (2010) Multi-cracks detection of a beamlike structure based on the on-vehicle vibration signal and wavelet analysis. J Sound Vib 329(21):4455–4465

49. Wanga YS, Leeb C-M, Kimb D-G, Xua Y (2007) Sound quality prediction for non-stationary vehicle interior noise based on wavelet pre-processing neural network model. J Sound Vib 299(4–5):933–947
50. Chatterjee P, OBrien E, Li Y, Gonzalez A (2006) Wavelet domain analysis for identification of vehicle axles from bridge measurements. Comput Struct 84(28):1792–1801
51. Sun T, Pei H, Pan Y, Zhang C (2011) Robust wavelet network control for a class of autonomous vehicles to track environmental contour line. Neurocomputing 74(17):2886–2892
52. Qiao Y-L, Zhao C-H, Song C-Y (2009) Complex wavelet based texture classification. Neurocomputing 72(16–18):3957–3963
53. Srinivasan D, Jin X, Cheu RL (2005) Adaptive neural network models for automatic incident detection on freeways. Neurocomputing 64:473–496
54. Liu P (2009) A self-organizing feature maps and data mining based decision support system for liability authentications of traffic crashes. Neurocomputing 72(13–15):2902–2908
55. Robbersmyr KG (2004) Calibration test of a standard Ford Fiesta 1.1l, model year 1987, according to NS-EN 12767. Technical Report 43/2004, Agder Research, Grimstad
56. Huang M (2002) Vehicle crash mechanics. CRC Press, Boca Raton
57. ISO 6487:2000. Road vehicles—measurement techniques in impact tests—instrumentation
58. Chon KH, Cohen RJ (1997) Linear and nonlinear ARMA model parameter estimation using an artificial neural network. IEEE Trans Biomed Eng 44(3):168–174
59. Vien NA, Yu H, Chung TC (2011) Hessian matrix distribution for Bayesian policy gradient reinforcement learning. Inf Sci 181(9): 1671–1685
60. Nasoz F, Lisetti CL, Vasilakos AV (2010) Affectively intelligent and adaptive car interfaces. Inf Sci 180(20):3817–3836
61. Guo ZX, Wong WK, Li M (2012) Sparsely connected neural network-based time series forecasting. Inf Sci 193:54–71
62. Mendrok K (2010) Signal analysis and identification—lectures. AGH University of Science and Technology, Kraków
63. Grossman A, Morlet J (1984) Decomposition of Hardy functions into square integrable wavelets of constant shape SIAM. J Math Anal 15(4):723–736
64. Burrus CS, Gopinath RA, Guo H (1998) Introduction to wavelets and wavelet transforms. Prentice Hall, Upper Saddle River
65. Scargle JD, Steiman-Cameron T, Young K, Donoho DL, Crutchfield JP, Imamura J (1993) The quasi-periodic oscillations and very low frequency noise of Scorpius X-1 as transient chaos—a dripping handrail? Astrophys J Part 2 Lett 411(no.2):91–94
66. Misiti M, Misiti Y, Oppenheim G, Poggi J-M (2002) Wavelet Toolbox for use with MATLAB®—user's guide, ver. 2. The MathWorks Inc
67. Lin J, Qu L (2000) Feature extraction based on morlet wavelet and its application for mechanical fault diagnosis. J Sound Vib 234(1):135–148